

Abstract

The Integrated Fuel-Coolant Interaction (IFCI) computer code is being developed at Sandia National Laboratories to investigate the fuel-coolant interaction (FCI) problem at large scale using a two-dimensional, four-field hydrodynamic framework and physically based models. IFCI will be capable of treating all major FCI processes in an integrated manner. This document is a product of the effort to generate a stand-alone version of IFCI, IFCI 6.0. The User's Manual describes in detail the hydrodynamic method and physical models used in IFCI 6.0. Appendix A is an input manual, provided for the creation of working decks.

Table of Contents

Abstract.....	iii
Table of Contents	v
List of Figures	vi
List of Tables	vi
Acknowledgments	vii
Nomenclature	viii
1 Introduction	1
1.1 The Integrated Fuel-Coolant Interaction Code.....	1
1.2 Existing Documentation	1
1.3 Scope of Report	1
1.4 The Fuel-Coolant Interaction Event	1
1.5 Other FCI Modeling.....	2
2 IFCI Overview.....	4
2.1 General Description	4
2.2 Code Structure	5
2.3 Input and Output	5
3 Basis and Assumptions	7
3.1 Field Equations	7
3.2 Equations of State	8
3.2.1 Water-Steam.....	8
3.2.2 Noncondensable Gases	9
3.2.3 Melt.....	9
3.3 Closure Equations and Constitutive Relations	9
3.3.1 Interfacial Friction Coefficients	10
3.3.2 Interfacial Areas	10
3.3.3 Heat Transfer Coefficients.....	10
3.3.3.1 Bulk Boiling	10
3.3.3.2 Film Boiling.....	11
3.4 Additional IFCI Models	11
3.4.1 Melt Fragmentation Model	12
3.4.2 Melt Surface Area Convection Model.....	12
3.4.3 Melt Surface Area Tracking Model.....	15
3.4.3.1 Computation of Slope	16
3.4.3.2 Computation of Cell Interfacial Area	17
4 Quality Assurance.....	18
4.1 Models and Correlations	18
4.1.1 Stripping Model.....	18
4.1.2 Flow Regimes.....	18
4.1.3 Film Boiling Model	18
4.2 Comparison of Code Results with Experimental Data	18
4.3 Model Limitations.....	18
4.4 Coding Methods.....	19
References.....	20
Appendix A : Input Description	23
Appendix B : Stripping Model.....	46

List of Figures

2.1 Hierarchy of IFCI Modules	6
3.1 IFCI Finite Difference Cell	14
B.1 Single Stage Drop Fragmentation	47
B.2 Rayleigh-Taylor Wave Crest Entrainment	51

List of Tables

3.1 Field Equations Solved by IFCI	7
3.2 Water Equation of State Limits	8
A.1 S.I. Units Used For IFCI	24
B.1 Comparison of Drag Coefficient Correlations	48
B.2 Air-Water Drops Shock Parameters	49
B.3 Normalized Drop Displacement: x/D_0 Comparison of Model Predictions With Experiment Data	49
B.4 Normalized Breakup Time, T^+ , Comparison of Model Predictions with Experimental Data	50
B.5 Normalized Fragment Size, d/D_0 , Comparison of Model Predictions with Experimental Data	50

Acknowledgments

The authors of this manual would like to thank several members of the Sandia National Laboratories Staff for their assistance in the review and preparation of this document, particularly David. C. Williams, Kevin W. Boyack and Eden L. Tadios. The efforts and expertise of Martin Pilch in a variety of areas critical to this project are greatly appreciated. Gratitude is also expressed to John Murphy and Michael Corradini for their work with the code and documentation. Their insight has proven invaluable. The USNRC, Office of Regulatory Research is acknowledged for their sponsorship of this work, and other fuel-coolant interaction research. Finally, the authors wish to thank Dr. Thomas J. Walker, USNRC, for his technical guidance of this program.

Nomenclature

A	=	cell-centered flow area (m ²)	Subscripts	
A _r	=	radial cell flow area (m ²)		
A _v	=	interfacial area per unit volume (m ² /m ³)	1-4	= fields 1 through 4 (vapor, water, solids, and melt, respectively)
A _z	=	axial cell flow area (m ²)	c	= critical
C	=	drag coefficient (Pa-s ² /m ³), or specific heat capacity J/kg-K	d	= discrete
C _v	=	liquid specific heat at constant volume (J/kg-K)	f	= continuous fluid
C _p	=	liquid specific heat at constant pressure (J/kg-K)	fc	= forced convection
D	=	drop diameter (m)	g	= gas
D _{AB}	=	binary diffusion coefficient, m ² /s	i	= interface
F ^v	=	virtual mass force (N/m ³)	j,k	= field 1 - 4
H	=	enthalpy at saturation (J/kg)	l	= liquid water
H _{lg}	=	latent heat of evaporation (J/kg)	m	= melt
M _v	=	molecular weight of vapor (steam) (kg/kmol)	nat	= natural convection
N	=	number of primary fragments	nc	= natural convection
P	=	pressure (Pa)	p	= primary
Q	=	energy transfer term (W/m ³)	r	= radial direction or relative
T	=	temperature (K)	rad	= radiation
T ⁺	=	dimensionless breakup time = $v_t t / D \epsilon^{1/2}$	s	= structure or saturation
a	=	adiabatic sound speed (m/s)	sat	= saturation
c	=	concentration of steam (kmol/m ³)	sub	= subcooled
g	=	gravitational acceleration (m/s ²)	v	= vapor (steam)
h	=	heat transfer coefficient (W/m ² -K), or enthalpy (J/kg)	w	= wall or structure or melt
k	=	thermal conductivity (W/m-K)	z	= axial direction
t	=	time (s)	∞	= bulk fluid
u or e	=	internal energy (J/kg)		
v	=	velocity (m/s)	Superscripts:	
\vec{v}	=	velocity vector (m/s)	°	= reference quantity
Γ	=	mass transfer rate (kg/m ³ -s)	c	= convective
Γ _e	=	entrainment surface area generation rate (m ² /m ³ -s)	•	= value at end of EOS table range
Γ _p	=	primary surface area generation rate (m ² /m ³ -s)		
α	=	volume fraction		
β	=	thermal expansion coefficient (K ⁻¹)		
ε	=	density ratio = ρ_∞ / ρ_d		
ρ	=	density (kg/m ³)		
σ	=	surface tension (Pa-m), or Stefan-Boltzmann constant (W/m ² -K ⁴)		
μ	=	dynamic viscosity (kg/m-s)		
ν	=	kinematic viscosity (m ² /s)		
ΔT _w	=	T ₄ - T _s		
ΔT _{sub}	=	T _{sat} - T ₂		
ΔT _v	=	T _{sat} - T ₁		
Nu	=	Nusselt number, hD/k		
Pr	=	Prandtl number = C _p μ/k		
Re	=	Reynolds number = vD/ν		
We	=	Weber number = ρv ² D/σ		

1. Introduction

The Integrated Fuel-Coolant Interaction Code (IFCI) is a best-estimate computer program for analysis of phenomena related to mixing of molten nuclear reactor core material with reactor coolant (water). The stand-alone version, IFCI 6.0, of the code has been designed for analysis of small- and intermediate-scale experiments in order to gain insight into the physics (including scaling effects) of molten fuel-coolant interactions (FCIs), and to assess and validate the code's methods, models, and correlations.

IFCI is under development at Sandia National Laboratories (SNL) sponsored by the United States Nuclear Regulatory Commission, Office of Nuclear Regulatory Research (USNRC/RES).

This version of the code has been demonstrated to be operational in the IFCI 6.0 Operational Assessment Report.^a A thorough validation effort is planned for the near future. The USNRC/RES, SNL, other USNRC contractors, and other interested parties will be contributing to the validation effort. That report is being issued so that all validation efforts will have a published and common basis for input preparation.

This document consists of the technical description of all major models, correlations, and pertinent equations in IFCI 6.0. It also identifies limitations of the IFCI models. The input description addresses all input parameters, files, and discusses the impact of certain key parameters on results. Users may also refer to the IFCI 6.0 Operational Assessment.^a

1.1 The Integrated Fuel-Coolant Interaction Code

The IFCI computer code is developed to investigate FCIs in as mechanistic a manner as possible. The code is intended to address all aspects of FCI phenomena, including coarse fragmentation and mixing of molten material with water, triggering, propagation and fine fragmentation, and expansion of the melt-water system. The ultimate objective of the code is to predict rates of steam generation, melt fragmentation and dispersion, shock wave generation and propagation, and system loading for explosive and non-explosive FCIs. The intent is to study and assess FCI scenarios for nuclear reactors and other industrial applications.

^a Letter Report from F. J. Davis to USNRC, dated November 1, 1993.

1.2 Existing Documentation

Young (1987) and Dosanjh (1989) describe an early version of the IFCI code. Much of the material in these two documents on IFCI's surface area transport logic, dynamic fragmentation model, and equation-of-state package is still current. Young (1990) describes a recent code version which includes a melt surface entrainment model and a melt surface tracking algorithm. All three references describe results of IFCI runs that model a generic version of an intermediate-scale FCI pouring mode experiment in the Fully Instrumented Test Series (FITS). (Mitchell et al. 1981; Corradini 1981a; Marshall 1988) These IFCI runs served three main purposes: 1) to demonstrate that the code architecture is essentially complete and functional; 2) to provide an early qualitative assessment of the operability of the underlying models and constitutive relations, and; 3) to improve perspective on the needs for and priorities of further model development and experimental data.

Complementary to this report is an Operational Assessment Report (OAR) for the IFCI code.^a The OAR discusses actual calculations which address the performance of the IFCI code.

1.3 Scope of Report

This document describes the stand-alone version of the IFCI code (IFCI 6.0). Included are detailed descriptions of the hydrodynamic field equations and closure relations, and the models used to describe FCI phenomena, notably models for dynamic fragmentation (including surface entrainment), surface area transport, and surface tracking. Parametric detonation/fine-fragmentation models have also been implemented, and are described in detail here. At present, these models have been incorporated into IFCI but not fully validated.

1.4 The Fuel-Coolant Interaction Event

It is generally agreed that the FCI process can be roughly divided into four phases: the initial coarse mixing phase, the trigger phase, the detonating propagation phase, and the hydrodynamic expansion phase. These four phases are useful conceptually, although in reality they may all be occurring simultaneously in different spatial locations in the melt-coolant mixture region. In addition to the four phases, there are also different contact modes that must be considered: the pouring mode, in which a mass of molten material is dropped into a pool of coolant; jet mixing,

Introduction

where a jet of melt is injected into coolant; and the stratified mode, where the melt is in a pool or layer, covered by a layer of coolant.

Coarse mixing is characterized by entry of molten material (melt) into a coolant (water) with accompanying vapor generation, intermixing of the melt, water, and vapor, and breakup of the melt into smaller diameter drops (smaller meaning of order 0.1-10 cm); this phase occurs on a time scale of 0.1-1.0 s. During this phase, the melt and water are insulated from one another by a vapor film, which serves to maintain the fuel temperature close to its initial value throughout coarse mixing. Breakup of the melt is thought to be governed by hydrodynamic instabilities, notably the Rayleigh-Taylor and Kelvin-Helmholtz instabilities. These breakup processes are driven by relative velocity differences or accelerations between the melt and the water/steam interface.

Triggering occurs when some local disturbance collapses the vapor films around the melt. This collapse allows direct water-melt contact or near contact, high heat transfer rates to the water, and high relative velocities in the vicinity of the trigger. If the triggering event is sufficiently strong and conditions in the mixture are favorable, the mixture may enter a detonating propagation phase. Triggering is not well understood, but is typically observed to occur quickly, on a time scale of around 100 μ s, and is often initiated by contact of the melt with a solid surface. (Young 1987; Kim 1985; Corradini 1981b; Kim and Corradini 1988)

The explosive propagation phase is characterized by a "reaction zone" which propagates through the mixture region. Within this reaction zone, the coarsely mixed melt is rapidly fragmented into particles in the 10-100 μ m size, with accompanying rapid increase in melt surface area, release of heat to the water and generation of shock waves. It should be noted that liberation of chemical energy is not accounted for at this time. Typical experimentally observed propagation speeds are in the 50-500 m/s range. (Mitchell et al. 1981; Corradini 1981a) The same hydrodynamic instabilities which are present during coarse mixing could also be responsible for the rapid fine fragmentation occurring during propagation, although other mechanisms may also be operative, for instance, jet penetration of the melt by the water (Marshall 1988) or shock-wave induced fragmentation.

In the expansion phase, the expanding steam-water-melt mixture converts thermal energy into work on the surroundings. This phase has been treated in detail by various researchers. (Swenson and Corradini 1981; Stevenson 1980)

1.5 Other FCI Modeling

Past research on FCI phenomena has been both experimental and theoretical in nature, but has not totally succeeded in resolving questions on FCI effects at large scale. In general, most of this research has been directed to answer questions of reactor safety. Separate effects and integrated experiments have been performed at small and intermediate scales to investigate many FCI phenomena. These experiments have provided much useful information, but must be much smaller than actual reactor or industrial scales. FCIs have demonstrated scale-dependence in past experiments, for instance, the "pint theory" (Mitchell et al. 1981) lower limit on the amount of melt necessary for an FCI, and there are very likely other scale-dependent processes in FCIs that are unknown at this time, making the extrapolation of experimental data to industrial scale very uncertain. On the theoretical side, lack of data on basic FCI phenomena makes choosing the correct model from among competing models very difficult; without an accurate model of the physical phenomena occurring during an FCI, the experimental results cannot be confidently extended to large scale.

Early models and correlations tended to be parametric and address only isolated aspects of FCIs. As more knowledge of FCIs was gained, models evolved to include more physics. Simultaneously, advances in computational hydrodynamics allowed incorporation of the more refined models in a suitable hydrocode framework, allowing more aspects of the FCI to be treated simultaneously in an integrated fashion.

These modeling efforts with hydrocodes have also evolved from simple models and one-dimensional, single field hydrocodes towards more physical models and two-dimensional, multifield hydrocodes. This evolution has taken place both as the limitations of early modeling efforts were recognized and as more advanced computational hydrodynamic techniques have become available.

Recent FCI modeling efforts have generally been aimed at either the coarse mixing phase or the detonation phase. Examples of coarse mixing calculations are those done by Bankoff and Hadid (1984), Abolfadl and Theofanous (1987), Thyagaraja and Fletcher (1986), and Chu and Corradini (1989), all for mixing in the lower plenum of a power reactor. Examples of propagation calculations are those of Carachalios et al. (1983), Medhekar et al., (1988), and Fletcher and Thyagaraja (1989). The above efforts generally have made simplifying assumptions, either in the hydrodynamic model or in the models of FCI phenomena, to make the problem more tractable. Several of the coarse mixing calculations, for instance, use a

constant initial particle size (Bankoff and Hadid 1984; Abolfadl and Theofanous 1987; Thyagaraja and Fletcher 1986), an assumption that incorrectly predicts early steam generation rates and consequent early separation of melt and coolant. The propagation calculations mentioned above are one-dimensional.

2. IFCI Overview

Before describing the details of IFCI, it will be helpful to have a general understanding of the code and how it operates. Section 2 provides a general description of the IFCI code, a description of IFCI's code structure, and a brief description of IFCI's inputs and outputs.

2.1 General Description

The current state of knowledge about the physical processes occurring in FCIs, characteristics of existing hydrocodes, and the necessity of calculating FCIs in a reactor safety context were all considerations in the original design of IFCI. IFCI 6.0 has been modified to provide useful insight and a usable analysis tool for the study of FCIs. Therefore, to make IFCI more user-friendly, the stand-alone version is void of code references and specific reactor structures which are extraneous to FCI phenomena and progression of FCI events.

Because of the radically different time scales associated with the different phases of an FCI, an implicit numerical hydrodynamics method is desirable for its ability to exceed the Courant limit (Roache 1972), thereby reducing computation time. The presence of at least three separate material fields in the FCI problem (water, vapor, and molten fuel), all at different temperatures and moving at different velocities, also suggested the use of a multifield method. The presence of shock waves during the propagation phase requires use of a compressible hydrodynamic method.

The Stability-Enhancing Two-Step (SETS) method (Mahaffy 1982; Dearing 1985) was chosen as an appropriate hydrodynamic method that satisfied the above criteria. This selection was also motivated by the existence of MELPROG/MOD1 (Dosanjh 1989; Kelly 1985), a severe reactor accident code using the SETS method, which features a two-dimensional, four-field fluids compressible hydrodynamics module with many necessary models already incorporated. Although IFCI has been stripped of the MELPROG/MOD1 computer modeling software, the SETS method has been maintained.

MELPROG/MOD1 was designed to calculate the events occurring during a hypothetical core meltdown accident in a light-water reactor (LWR). This code already includes a phase change model, a sophisticated heat transfer model with complete boiling curve, an equation-of-state for steam and water, a flow regime map for both vertical and horizontal flow, and models for both interphase and field-structure drag. As such, MELPROG/MOD1 could be used

as the basis for IFCI, with the addition of models for FCI phenomena not covered by MELPROG/MOD1.

IFCI 6.0 consists of several modules, divided according to responsibility for calculating different physical processes, which respectively handle fluids transport, structure mechanical and thermal response (wall, plates), thermal radiation transport, convection, boiling heat transfer, etc. Output data are available as printed output, and a binary graphics output file.

IFCI provides a two-dimensional, r-z geometry, four-field hydrodynamics model, whose fields consist of vapor (steam), water, solid fuel, and melt (in IFCI, these are referred to as fields 1, 2, 3, and 4 respectively). A "field," in the context of the SETS method, means a set of momentum, mass continuity, and energy equations; a separate set of these equations is solved for each "field." Mass, energy, and momentum transfer between fields is represented by coupling terms in these equation sets.

IFCI is based on a two-dimensional, four-field implementation of the SETS hydrodynamic method. Use of a multifield method with separate mass, momentum, and energy equations for each field allows slip between the various materials (vapor, liquid coolant, and liquid melt), and a different temperature for each material. In IFCI the fields for melt and solid particulate at present are not coupled, therefore the solid particulate field is not used. IFCI uses an equation of state for water and steam obtained by fits to the steam tables (Los Alamos Safety Code Development Group, 1986) and a stiff gas equation of state for the melt. The constitutive relations required for the interfield coupling terms (heat transfer, momentum exchange, and phase change) include a bulk boiling model, a subcooled surface boiling model, a three-field flow regime map, and adaptations of standard heat transfer and momentum transfer correlations.

Additional models are included which are necessary to calculate phenomena that occur in FCIs. These are (1) a dynamic fragmentation model, which calculates the breakup, or change in effective diameter, of the melt based on local hydrodynamic conditions (densities and velocities), coupled with (2) a convection equation for melt surface area per unit volume; (3) a surface tracking model to follow the melt-coolant interface and, in particular, to calculate the melt characteristic length changes produced by large-scale (greater than finite-difference cell size) hydrodynamic motion of the melt; (4) a trigger model, to simulate a local explosion in a melt-water-steam mixture; and (5) a detonation-fine fragmentation model to calculate the rapid fragmentation and steam generation in a propagating reaction zone. It

appears, based on current understanding of FCIs, that these are the basic models necessary to calculate FCI phenomena; they may need to be supplemented later, as additional effects are discovered, but a code with these basic models should be capable of doing an adequate simulation of FCIs.

Other extensions necessary to IFCI include providing the interfield constitutive relations between the field for molten fuel ("melt") and the water and steam fields, and extending the equation-of-state package for water-steam to allow supercritical pressures and temperatures.

2.2 Code Structure

IFCI was formerly an integral part of the MELPROG code. It uses MELPROG's FLUIDS module hydrodynamics subroutines, extensively. Furthermore, IFCI drivers, input and output routines are derived from MELPROG subroutines. A description of MELPROG's code structure is given in Dosanjh (1989). However, at present, MELPROG's fluid fields for solids ("field 3") and melt ("field 4") are not coupled. In practice, MELPROG is run with the fields for water, steam, and solids (and a candling model) "on," and IFCI runs with water, steam and melt "on." Therefore, strictly speaking, IFCI is not a MELPROG module. IFCI's melt field is not coupled to MELPROG's DEBRIS or RADIATION modules.

Figure 2.1 shows the hierarchy of IFCI subroutines used for calculation of melt fragmentation, melt interface tracking, and melt surface area transport.

2.3 Input and Output

IFCI input routines for problem initialization and restart are derived from those used by MELPROG. An IFCI input deck is similar to that specified by MELPROG's Version 5.2 input description (Heames 1989). However, a number of extraneous parameters have been removed from the input and a number of additional quantities are required by routines FLDEOS, FRGMOD and TRGFICI, viz., melt reference mass fractions, reference pressure, and reference temperature, the square of the melt's inverse sound speed, fine fragmentation and trigger parameters (see Section 3.2.3 below).

IFCI generates two types of output; printed text and a fluids graphics file. The printed output is iteration information to standard output and text information for the fields, which includes, in addition to standard information (volume fraction, temperature, etc.), a characteristic diameter for melt particles that IFCI calculates for each mesh cell. The graphics file includes standard fluids

information, the melt characteristic diameter, and the melt surface area per unit volume for each mesh cell.

The fluid graphics file is usually input to a graphics post-processor, mpost, to produce contour plots of fluid variables. The file is formatted as an "unpacked comp file," and conforms to the input format for the TRAP postprocessor (Jenks and Martinez 1988) and can also be used with that program, if desired.

3. Basis and Assumptions

3.1 Field Equations

The equation set used in IFCI is a four-field, two-dimensional, cylindrical geometry version of a set commonly used in multifield computational hydrodynamics and originally derived from the general field equations of Ishii (Ishii 1975; Kocamustafaogullari 1971). A "field" in the context of multifield hydrodynamics is represented by separate momentum, mass continuity, and energy equations for each type and phase of material in the interaction. These three equations are solved for each "field." Mass, energy, and momentum transfer between fields are represented by coupling terms in the field equations for which constitutive relations must be provided. Also necessary is an equation of state for each field. The field equations, associated constitutive relations, equations of state, and initial and boundary conditions, are solved by use of the SETS method developed by Mahaffy (1982).

The field equations used in IFCI (Equations 3.1 through 3.4) are (for field k) given below in Table 3.1.

Finally, a constraint on the sum of the fluid volume fractions is also required:

$$1 - \sum_{j=1}^4 \alpha_j - \alpha_s = 0 \quad (3.5)$$

In equations 3.1 through 3.5, α_k is the volume fraction with respect to the total finite difference-mesh cell volume. There can also be a non-flow volume fraction in the cell, as structures, α_s . The velocity vector \vec{v}_k is composed of axial and radial components v_{zk} and v_{rk} . The third and fourth terms in Equation (3.1) represent mass transfer

among the fields and external mass source terms, respectively. The mass transfer between steam and liquid water is treated implicitly in temperature and pressure, while the other mass transfers are explicit sources. In the momentum equation [see Equation (3.2)], the fourth term represents momentum transfer between the fields, the fifth term represents wall friction, and the sixth term, F^v , is a virtual mass force, described in detail below. The coefficients, C , are evaluated explicitly based on the local flow regime. In the energy equation [see Equation (3.3)], the third term is the work term. The fourth term represents energy exchange between the fields due to phase change, with H_k representing the saturation enthalpy. The fifth term represents heat transfer between fields. The sixth term represents external energy sources, and the seventh term is energy transfer to an interface at saturation.

The virtual mass term F^v appearing in Equation (3.2) is used to add stability to the multifield equations. The form used here in Equation (3.4) is simplified from the full virtual mass expression as suggested in Bohl et al. (1987) and is applied only to discrete vapor flows. In Equation (3.4), $\bar{\rho}_L$ is an effective liquid density for the water, melt and solid fields, $\bar{\alpha}_k$ is a normalized liquid field volume fraction, and the virtual mass coefficient, C_{vm} , is set to a value giving stability to the equation set (No and Kazimi 1985),

$$C_{vm} = 4\sqrt{\bar{\alpha}_L^3 \bar{\alpha}_L \rho_L / \bar{\rho}_L} \quad (3.6)$$

Table 3.1 Field Equations Solved by IFCI

$\frac{\partial}{\partial t}(\alpha_k \rho_k) + \nabla \cdot (\alpha_k \rho_k \vec{v}_k) - \Gamma_{jk} - \Gamma_{wk} = 0$	(3.1)
$\frac{\partial}{\partial t} v_{xk} + \vec{v}_k \cdot \nabla v_{xk} + \frac{1}{r_k} \frac{\partial r}{\partial x} + \frac{1}{(\alpha \rho)_k} \left[\sum_{j=1}^4 C_{xjk} (v_{xk} - v_{xj}) v_{xk} - v_{xj} + C_{xwk} v_{xk} v_{xk} + F_{xk}^v \right] + g_x = 0$	(3.2)
$\frac{\partial}{\partial t}(\alpha_k \rho_k e_k) + \nabla \cdot (\alpha_k \rho_k e_k \vec{v}_k) + P \left(\frac{\partial \alpha_k}{\partial t} + \nabla \cdot \alpha_k \vec{v}_k \right) - \sum_{j=1}^4 \Gamma_{jk} H_k - \sum_{j=1}^4 Q_{jk} - Q_{wk} - Q_{sk} = 0$	(3.3)
$F_{xk}^v = \alpha_k \bar{\rho}_L C_{vm} \left[\frac{\partial v_{xk}}{\partial t} - \bar{\alpha}_2 \frac{\partial v_{x2}}{\partial t} - \bar{\alpha}_3 \frac{\partial v_{x3}}{\partial t} - \bar{\alpha}_4 \frac{\partial v_{x4}}{\partial t} \right]$	(3.4)

Equations 3.1 through 3.5 constitute a set of seventeen coupled, non-linear, partial differential equations that, along with material equations of state and constitutive relations for mass, energy and momentum exchange, form the hydrodynamic equation set of IFCI.

3.2 Equations of State

3.2.1 Water-Steam

The IFCI 6.0 equation of state (EOS) package for water-steam consists of a series of analytic fits to standard steam tables (Los Alamos Safety Code Development Group 1986). The water-steam EOS package in IFCI is driven by a subroutine named THERMO. THERMO has been modified for use in IFCI by adding analytic extensions at the limits of the original package. In normal operation, THERMO returns water and steam properties, plus property derivatives with respect to the independent variables, which are the water and vapor temperatures and the total and steam partial pressures. When the input variables exceed the limits of the regions over which the analytic fits are valid, THERMO returns the properties and derivatives at the limits. Unfortunately, the pressure iteration step in the SETS method, for this case, receives non-zero derivatives for properties that are actually not changing. Consequently, the pressure iteration will either fail or reduce the timestep drastically. Adding the analytic extensions to the THERMO package allows the properties to continue to change in agreement with the derivatives. The extensions were added, in part, because of the likelihood of generating supercritical conditions during the FCI explosion phase. They are also useful when superheated temperatures occur in water or vapor.

The limits in the THERMO package are shown in Table 3.2.

These limits are extended as follows:

1. If either the vapor temperature or pressure exceeds the table limits, then the vapor equation of state is extended assuming ideal gas behavior. The equation used is

$$\rho_s^i = \frac{P_s}{R_s T_v} \quad (3.7)$$

where,

ρ_s^i = ideal gas law steam density, kg/m³,
 P_s = steam partial pressure, Pa,
 R_s = gas constant for steam = 462 J/kg/K,
 T_v = vapor temperature, K.

The density from Equation 3.7 is joined smoothly to the table value at the limit by adding an offset

$$\Delta\rho = \dot{\rho}_s - \frac{\dot{P}_s}{R_s \dot{T}_v}, \quad \rho_s = \rho_s^i + \Delta\rho \quad (3.8)$$

where the overscript "·" refers to the table edge values and ρ_s is the steam density. This method works well provided that $\rho_s^i \gg \Delta\rho$. The derivatives of vapor density with respect to temperature and pressure are replaced by the ideal gas law derivatives if the independent variable exceeds the table limits. The pressure derivatives are

$$\frac{\partial \rho_s}{\partial P} = \frac{\rho_s}{P_s}, \quad P_s > \dot{P}_s \quad (3.9a)$$

or

$$\frac{\partial \rho_s}{\partial P} = \frac{\rho_s}{P_s} - \frac{1}{R_s \dot{T}_s} + \left(\frac{\partial \rho_s}{\partial P}(\dot{T}_s, P_s) \right), \quad P_s \leq \dot{P}_s \quad (3.9b)$$

The temperature derivatives are

$$\frac{\partial \rho_s}{\partial T_v} = \frac{\rho_s}{T_v}, \quad \text{for } T_v > \dot{T}_v \quad (3.10a)$$

or, for $T_v \leq \dot{T}_v$,

Table 3.2 Water Equation of State Limits

Minimum Hydrogen Partial Pressure	1 x 10 ⁻⁵ Pa
Minimum Steam Partial Pressure	1 Pa
Maximum Steam Partial Pressure	45 MPa
Minimum Vapor Temperature	273 K
Maximum Vapor Temperature	3000 K
Minimum Water Temperature	273 K
Maximum Water Temperature	713.9 K
Maximum Saturation Temperature	647 K

$$\frac{\partial \rho_s}{\partial T_v} = -\frac{\rho_s}{T_v} + \frac{\dot{P}_s}{R_s T_v^2} + \left(\frac{\partial \rho_s}{\partial T_v} (T_v, \dot{P}_s) \right) \quad (3.10b)$$

The steam internal energy, u_s , is extended using first order Taylor series expansions in T and P:

$$u_s = \dot{u}_s + \left(\frac{\partial u_s}{\partial T_v} \right) \Delta T_v + \left(\frac{\partial u_s}{\partial P} \right) \Delta P \quad (3.11a)$$

where

$$\Delta P = P_s - \dot{P}_s, \quad \Delta T_v = T_v - \dot{T}_v \quad (3.11b)$$

2. If either the liquid (field 2) temperature or the pressure exceed the table limits, then the liquid internal energy, u_2 , and density, ρ_2 , are extended using Taylor series in T and P:

$$u_2 = \dot{u}_2 + \left(\frac{\partial u_2}{\partial T_2} \right) \Delta T_2 + \left(\frac{\partial u_2}{\partial P} \right) \Delta P \quad (3.12a)$$

$$\rho_2 = \dot{\rho}_2 + \left(\frac{\partial \rho_2}{\partial T_2} \right) \Delta T_2 + \left(\frac{\partial \rho_2}{\partial P} \right) \Delta P \quad (3.12b)$$

where $\Delta T_2 = T_2 - \dot{T}_2$

The enthalpies of water and steam at saturation and the saturation temperature must also be extended in pressure, since the derivatives of these quantities, as originally calculated by THERMO, do not go to zero in the table at the critical point. In IFCI, they are allowed to keep changing slowly with pressure and multiplied by a function, f_h , that gradually decreases the change in the properties and the property derivatives to zero. The expressions for the enthalpies at saturation are

$$h_{1sat} = \dot{h}_{1sat} f_h, \quad (3.13a)$$

$$h_{2sat} = \dot{h}_{2sat} f_h, \quad \text{and} \quad (3.13b)$$

$$f_h = 1 + 10^6 \left(\frac{1}{\dot{P}_{sat}} + \frac{1}{P_{sat}} \right) \quad (3.13c)$$

where the subscript "sat" refers to saturation. The derivatives are given as

$$\frac{\partial h_{1sat}}{\partial P} = \frac{\partial \dot{h}_{1sat}}{\partial P} f_h - h_{1sat} \frac{10^6}{P_{sat}^2}, \quad (3.14a)$$

and

$$\frac{\partial h_{2sat}}{\partial P} = \frac{\partial \dot{h}_{2sat}}{\partial P} f_h - h_{2sat} \frac{10^6}{P_{sat}^2} \quad (3.14b)$$

Some modification of the liquid density routine was also required, as the fit used for the liquid density had a positive derivative with respect to temperature near the critical point. This was physically incorrect, and caused the heat transfer routines to calculate a negative Grashof number ($\beta g \Delta T D^3 / \nu^2$). The liquid temperature passed to the liquid density routine was restricted within IFCI to be less than the critical temperature to fix this problem.

3.2.2 Noncondensable Gases

Noncondensable gases are described by the ideal gas law [see Equation (3.7)].

3.2.3 Melt

A stiffened gas equation is used to provide the dependence of melt density, ρ_4 , on pressure:

$$\rho_4 = \frac{1}{a^2} P + \rho_4^\circ \quad (3.15)$$

where

a = adiabatic sound speed in the melt, and

ρ_4° = a nominal reference density for the melt.

3.3 Closure Equations and Constitutive Relations

The interfield heat transfer terms in Equation (3.3) are given as

$$Q_{jk} = A_{jk} h_{jk} (T_k - T_j) \quad (3.16)$$

where the interfacial area per unit volume between fields j and k, A_{jk} , and the heat transfer coefficient, h_{jk} , are provided by constitutive relations for each flow regime.

Mass transfer between the water and steam fields is described by a simple bulk boiling model assuming the existence of an interface between the two fields at the saturation temperature:

$$\Gamma_{12} = A_{12} \frac{h_{2sat} (T_2 - T_{sat}) - h_{1sat} (T_1 - T_{sat})}{H_{lg}} \quad (3.17)$$

Surface boiling at the melt surface is modeled by a subcooled surface boiling model,

$$\Gamma_4 = A_4 \frac{h_{4\text{sat}}(T_4 - T_{\text{sat}}) - h_{2\text{sat}}(T_{\text{sat}} - T_2)}{H'_{\text{lg}}} \quad (3.18)$$

where H'_{lg} is an effective latent heat of vaporization, modified to account for the sensible heat of the vapor. Equation (3.18) is used to describe film boiling at a surface with either saturated or subcooled coolant.

Constitutive relations are provided in IFCI for heat and momentum transfer in the bubbly, slug, and mist flow regimes between water and vapor. Flow regimes for the melt field are derived by treating the water and vapor together as a second phase. The melt is then described, based on the melt volume fraction, as either continuous with entrained vapor-water droplets, or as melt droplets in a continuous vapor-water phase. Provision is also made for the existence of mixture levels; i.e., formation of pools of water or melt.

Heat transfer coefficients (HTCs) between melt and water fields are provided via a boiling curve, which describes nucleate, transition, and film boiling. Only film boiling, the dominant regime for IFCI is described here. The complete boiling curve is described by Dosanjh (1989). At high vapor volume fractions, a transition is made between film boiling heat transfer to water and convective heat transfer to vapor from the melt.

3.3.1 Interfacial Friction Coefficients

The drag coefficients C_{jk} between fields j and k are written as

$$C_{jk} = \frac{3}{4} \rho_f \alpha_d \frac{C_f}{D} \quad (3.19)$$

where the subscripts f and d refer to the continuous fluid and discrete fields, respectively. The friction factor C_f is given by Bird et al. (1960),

$$C_f = \begin{cases} \frac{24}{\text{Re}} & , \text{Re} < 2 \\ \frac{18.7}{\text{Re}^{0.68}} & , \text{Re} \geq 2 \end{cases} \quad (3.20)$$

where the Reynolds number, Re , is based on the continuous field density and dynamic viscosity, ρ_f and μ_f , respectively, the relative velocity, v_r , and the characteristic diameter of the discrete field, D . The diameter, D , appearing in Equation (3.19) is based on a critical Weber number, We_c ,

$$D = \frac{\text{We}_c \sigma}{\rho_f v_r^2} \quad (3.21)$$

where We_c is 7.5 for bubbles, 4 for droplets of water, and 12 for melt or water-vapor (combined field) drops. (Liles et al. 1988) If a mixture level is present, then D is the axial hydraulic diameter. For melt, if the melt diameter is larger than the cell size, then a flat interface geometry is assumed and the melt size D_m is used for D .

3.3.2 Interfacial Areas

The interfacial area, A_{jk} , is calculated as

$$A_{jk} = \frac{6\alpha_d}{D} \quad (3.22)$$

if a discrete-continuous geometry is present, or the axial area of the cell divided by the cell volume, if the fields are stratified.

3.3.3 Heat Transfer Coefficients

Although there are many heat transfer coefficients provided in the IFCI constitutive relation routines corresponding to the many possible flow conditions, only those relevant to FCIs will be described, notably those associated with the bulk boiling and surface film boiling conditions.

3.3.3.1 Bulk Boiling

For bulk phase change, the heat transfer coefficients depend on whether the flow regime is bubbly, slug, or mist. The vapor-saturated-interface heat transfer coefficient is

$$h_{1\text{sat}} = \begin{cases} 1000, \alpha \leq 0.3 \\ \text{slug}, 0.3 < \alpha \leq 0.5 \\ \text{transition}, 0.5 < \alpha \leq 0.75 \\ \text{Nu} \frac{k_v}{D}, 0.75 < \alpha \leq 1 \end{cases} \quad (3.23)$$

The Nusselt number, Nu , appearing in Equation 3.23 is a sphere convection Nusselt number. (Lee and Ryley 1968) The heat transfer coefficients in the slug and transition flow regimes are determined by a combination of the values for the bubbly and mist flow regimes.

$$\text{Nu} = 2 + 0.74\sqrt{\text{Re}} \quad (3.24)$$

The water-saturated interface HTC is

$$h_{2\text{sat}} = \begin{cases} \text{Nu}_2 \frac{k_2}{D}, \alpha \leq 0.3 \\ \text{slug}, 0.3 < \alpha \leq 0.5 \\ \text{transition}, 0.5 < \alpha \leq 0.75 \\ 0.02 \rho_2 C_v v_r, 0.75 < \alpha \leq 1 \end{cases} \quad (3.25)$$

where C_v is the liquid specific heat at constant volume.

In the above expression for h_{2sat} , the Nusselt number Nu_2 is the greater of a sphere forced convection Nusselt number [see Equation (3.24)] or one derived from the Plesset-Zwick bubble growth formula (Mikic et al. 1970),

$$Nu = \frac{12}{\pi} \Delta T_{sub} \left[\frac{\rho_l \left(\frac{\partial e_l}{\partial T_l} \right)}{\rho_v H_{vf}} \right]. \quad (3.26)$$

The formula for $a > 0.75$ is derived assuming that $Pr = 1$ and $C_v = C_p$, the liquid specific heat at constant pressure.

3.3.3.2 Film Boiling

The film boiling HTC for the melt is given as

$$h_{4s} = \max\{h_{free}, h_{fc}\} + h_{rad}, \quad (3.27)$$

where the h_{free} and h_{fc} are subcooled boiling correlations from Dhir and Purohit (1977):

$$h_{free} = h_{sat} + h_{nat} \frac{\Delta T_{sub}}{\Delta T_w}, \quad (3.28)$$

where h_{sat} is given by the Bromley correlation, (Bromley et al. 1953)

$$h_{sat} = 0.8 \left\{ \frac{g \rho_v (\rho_l - \rho_v) H_{vf} k_v^3}{\mu_v D \Delta T_w} \right\}^{1/4}, \quad (3.29)$$

and h_{nat} is a natural convection correlation,

$$h_{nat} = 0.9 \left\{ \frac{g \rho_v^2 C_{pl} \Delta T_{sub} k_l^3}{\mu_l D} \right\}^{1/4}. \quad (3.30)$$

h_{fc} is a combination of a saturated boiling HTC, h_{sat} and a forced convection HTC,

$$h_{fc} = h_{sat} + 0.8 \sqrt{Re} \left(1 + \frac{k_l}{k_v} \frac{\Delta T_{sub}}{\Delta T_w} \right) \frac{k_l}{D}. \quad (3.31)$$

The HTC for convection from the film interface to the bulk liquid water is given by the greater of a natural convection HTC or a forced convection HTC. (Bird et al. 1960)

$$h_{2s}^c = \max\{Nu_{nc}, Nu_{fc}\} \frac{k_l}{D}, \quad (3.32)$$

where

$$Nu_{nc} = 2.0 + 0.6 Gr^{1/4} Pr^{1/3} \quad (3.33a)$$

and

$$Nu_{fc} = 2.0 + 0.6 Re^{1/2} Pr^{1/3} \quad (3.33b)$$

Heat transfer from the melt to the vapor in film boiling is derived from the amount of heat given to the vapor as sensible heat:

$$h_{14} = \frac{\Gamma_4}{\Delta T_v} (0.1 C_{pv} \Delta T_v) \quad (3.34)$$

where C_{pv} is the vapor specific heat at constant pressure.

The radiation HTC h_{rad} is given as

$$h_{rad} = \sigma \varepsilon \frac{(T_4^4 - T_2^4)}{(T_4 - T_2)}. \quad (3.35)$$

3.4 Additional IFCI Models

In IFCI, a melt drop is described by an Eulerian melt field interacting with the water and steam fields, which are also Eulerian. The fuel characteristic size may either be smaller than a finite difference mesh cell (i.e., subgrid size) or extend over more than one cell. In the subgrid case, the fuel melt exists as discrete drops, which IFCI treats with models for primary breakup and surface entrainment, as described in Section 3.4.1. The primary breakup and surface entrainment models provide source terms for a continuity (transport) equation for melt volumetric surface area. Transport of melt volumetric surface area is described in detail in Section 3.4.2. In the case where the melt extent is larger than the finite difference grid, surface area generation takes place as the melt geometry distorts due to hydrodynamic motion on the grid. IFCI uses a surface area tracking model/algorithm to treat this case; it is described in Section 3.4.3. In addition for this case, the surface entrainment subgrid fragmentation model is used in cells containing a melt-water interface.

3.4.1 Melt Fragmentation Model

The idea of a dynamic fragmentation model which calculates the characteristic melt diameter as a function of instantaneous hydrodynamic conditions was first proposed by Camp (Young et al. 1979). A model using this idea was later incorporated into a version of the TEXAS one-dimensional FCI code (Young 1982) by Chu and Corradini (1989) using an empirical correlation derived from data obtained in the Sandia FITS experiments. (Rightley 1991) The fragmentation model in IFCI is a version of a dynamic fragmentation model developed by Pilch (1981) based on Rayleigh-Taylor instability theory and the existing body of gas-liquid and liquid-liquid drop breakup data.

The basic Pilch model describes primary breakup of a drop via penetration of the drop by Rayleigh-Taylor waves, and is expressed as

$$\frac{dD}{dt} = -\frac{(1 - N^{-1/3})}{T^+} |v_r| \epsilon^{0.5} \quad (3.36)$$

This formulation was developed from the empirical observation that, in high Weber number drop breakup experiments, the drop experiences primary breakup into 3-5 primary fragments in a dimensionless time T^+ between 1 and 1.25. While primary breakup is occurring, smaller fingers continuously develop and break off, forming a cloud of droplets. This effect is included in IFCI via a surface entrainment model

$$\frac{dS}{dt} = C_0 C_f^{0.75} \frac{1}{D} We^{0.25} |v_r| \epsilon^{0.5} \quad (3.37)$$

where $\frac{dS}{dt}$ is the surface entrainment rate per unit melt area, and C_0 is a constant 0.089. A more detailed derivation of the fragmentation model and a comparison to experimental data can be found in Appendix B.

Equations (3.36) and (3.37) are used in the formulation of surface area source terms for a melt volumetric-surface-area transport equation, as described in Section 3.4.2.

The drop breakup data from which Equations (3.36) and (3.37) were derived consisted of isothermal liquid-gas and liquid-liquid breakup data. It is assumed here that this correlation will also apply under boiling conditions. There is some justification for this assumption in the experiments of Greene, Ginsberg, and Tutu (1985), in that the drag coefficients for heated (boiling) and isothermal (nonboiling) steel balls dropped into water were about the same. Since the drag coefficient is essentially unchanged, the model is assumed to hold for both boiling and isothermal systems. A more important effect of boiling on the overall breakup is to cause higher local relative velocities and pressure fluctuations, accelerating the breakup process. This effect is included via the use of local relative velocity, v_r , in the equations.

3.4.2 Melt Surface Area Convection Model

In IFCI, the quantity convected with the melt is surface area per unit volume (volumetric surface area). (Ishii 1975) Therefore, the fragmentation mechanisms described by Equations (3.36) and (3.37) are reformulated in terms of rate of change of surface area per unit cell volume. This surface area formulation allows treatment of jets, drops, and other more general flows. The conversion to the volumetric surface area generation rate requires a knowledge of the relation between volumetric surface area

A_m and characteristic diameter D . In the case of discrete drops, this is given by

$$A_m = \frac{6\alpha_m}{D} \quad (3.38)$$

Differentiating the expression for volumetric surface area leads to an equation for the rate of change of A_m in terms of the rate of change of diameter for the primary breakup model [Equation (3.36)],

$$\Gamma_p = \frac{dA_m}{dt} = -\frac{6\alpha_m}{D^2} \frac{dD}{dt} = -A_m \frac{1}{D} \frac{dD}{dt} \quad (3.39)$$

where Γ_p = surface area source due to primary breakup (m^2/m^3-s). In the case of the surface entrainment rate per unit melt area dS/dt , simply multiplying this rate by the volumetric melt area A_m gives the volumetric entrainment rate Γ_e . These surface generation rates are used as surface area source terms in a continuity equation for A_m ,

$$\frac{\partial A_m}{\partial t} + \nabla \cdot (v_m A_m) = \Gamma_p + \Gamma_e \quad (3.40)$$

After solving the surface area transport Equation (3.40) for a timestep, new values of the characteristic melt diameter are calculated from the new surface area by reversing the procedure in Equation (3.38). The present formulation of the surface area transport allows only one melt characteristic-diameter per cell, which is assumed to represent a mean value of the actual size distribution in the cell.

The numerical formulation of the surface area source must be done carefully so that the relation between surface area and melt diameter is preserved. In IFCI, a "staggered" mesh cell is used, where the velocities are defined on the cell edges, and densities, volume fractions, drop diameter, the volumetric surface area (and hence the surface area source term), are defined at the cell center (see Figure 3.1).

Another consideration peculiar to the SETS method in IFCI is that, for numerical reasons, there is a minimum volume fraction, dependent on problem geometry and nodalization, in a cell for each field, even if the field is not actually present; this minimum volume fraction must be taken into account when forming averages of field densities and volume fractions on cell boundaries for use in the breakup model, so that the actual property values are not swamped by spurious residual values in the empty cells. An example is provided later in this section.

The primary fragmentation model is set up in IFCI by first calculating the rate of change of diameter on each of a cell's edges. The rate is calculated only if both the melt field and at least one other field are present in the two cells adjoining a given edge. The cell-centered quantities

are averaged so that the averaged quantity will go to the correct limit under bounding conditions, for instance one cell full of melt and the adjoining cell full of water.

The following description of the finite difference formulation for the averages is written in terms of averages on the top cell edge; averages on the bottom and in the radial direction are done in a completely analogous fashion.

The volume fractions on the edge are formed as the simple arithmetic average,

$$\bar{\alpha}_1 = \frac{\alpha_{1ij} + \alpha_{1ij+1}}{2}, \quad \bar{\alpha}_2 = \frac{\alpha_{2ij} + \alpha_{2ij+1}}{2} \quad (3.41)$$

where

- $\bar{\alpha}_1$ = average volume fraction for field 1 (vapor) on the top edge of cell (i,j),
- $\bar{\alpha}_2$ = average volume fraction for field 2 (water) on the top edge of cell (i,j),
- i = radial cell index,
- j = axial cell index,
- α_{kij} = cell volume fraction for field k in cell (i,j).

The water and vapor field densities are first averaged separately by weighting with the cell volume fractions in the two cells to give effective water and vapor densities on the cell edge,

$$\bar{\rho}_k = \frac{\alpha_{kij} \rho_{kij} + \alpha_{kij+1} \rho_{kij+1}}{\alpha_{kij} + \alpha_{kij+1}} \quad (3.42)$$

The effective fluid density ρ_f for use in the breakup correlation is then formed by weighting the effective edge densities with the respective edge volume fractions,

$$\rho_f = \frac{\bar{\alpha}_1 \bar{\rho}_1 + \bar{\alpha}_2 \bar{\rho}_2}{\bar{\alpha}_1 + \bar{\alpha}_2} \quad (3.43)$$

This procedure is used so that if, for instance, one cell is full of water and the other contains melt, the fluid density calculated will be equal to the water density, rather than one-half the water density. The effective fluid velocity is calculated as the effective-mass-weighted velocity normal to the edge, so that, for the example case, the axial velocity is the one used. This choice is the correct one for the present Rayleigh-Taylor model, which is driven by accelerations normal to the interface between the melt and fluid, whereas other instabilities, such as Kelvin-Helmholtz, would be driven by tangential velocities. The fluid velocity is given as

$$v_f = \frac{\bar{\alpha}_1 \bar{\rho}_1 v_1 + \bar{\alpha}_2 \bar{\rho}_2 v_2}{\bar{\alpha}_1 \bar{\rho}_1 + \bar{\alpha}_2 \bar{\rho}_2} \quad (3.44)$$

where

- v_f = fluid velocity (m/s),
- v_{zk} = axial velocity for field k on top edge of cell (m/s).

The effective melt characteristic size used in the rate model on the cell edge is formulated as

$$\bar{D} = (\alpha_{mij} + \alpha_{mij+1}) \left[\frac{\alpha_{mij}}{d_{ij}} + \frac{\alpha_{mij+1}}{d_{ij+1}} \right]^{-1}. \quad (3.45)$$

This formulation is appropriate for the transported quantity, volumetric surface area, which is proportional to $1/D$, and also allows handling of the minimum volume fraction cutoff used in the IFCI numerics. The minimum volume fraction is typically 10^{-5} . Cells in which fields are turned off have the corresponding volume fraction set to a minimum ten times smaller. This means that cells also have a minimum volumetric surface area, whether there is actually any melt in them or not. We would like this residual surface area to be a small number; in particular, the residual area should be small in comparison to the amount of surface area fluxed into an empty cell during one timestep. If these conditions are not met, then the incoming surface area can be swamped by the residual amount in the receiving cell. This is prevented in IFCI by setting the initial diameter in empty cells to a large number, on the order of 10^5 m.

Setting the initial melt diameter in empty cells to a large number is another good reason for the inverse averaging procedure, as a simple average would be swamped by the large value. If one cell is full and the adjoining one is empty on an edge, the geometric average goes to the melt diameter of the full cell, which is the desired result.

The quantity calculated on the cell edges is actually the rate of change of diameter divided by the effective diameter; this quantity is weighted by the effective melt volume fraction for each edge and used to form an effective rate of change for the cell,

$$\Gamma_A = -A_v \frac{\sum_{n=1}^4 \bar{\alpha}_n \left(\frac{1}{D} \frac{dD}{dt} \right)_n}{\sum_{n=1}^4 \bar{\alpha}_n} \quad (3.46)$$

where the sum on n goes over the four cell edges.

The above expression for rate of change of volumetric surface area in a cell due to Rayleigh-Taylor instabilities is then used as a source in the surface area transport equation. After calculation of the new surface area using the transport equation, the new melt diameter is obtained using the relation between diameter, volume fraction, and surface area.

3.4.3 Melt Surface Area Tracking Model

Multifield hydrodynamic methods are generally used to model problems involving interpenetrating phases. The

details of the interpenetration, or mixing, occur at a smaller scale than the finite difference grid cell size and are contained in the interfield exchange coefficients. These details include the local interfacial area and characteristic lengths of the mixing fluids. The interfacial areas and length scales may be either calculated in some manner, as from flow regime maps and constitutive relations involving a critical Weber number and flow geometry, or the flow regime and associated parameters may be constant, user-input values.

For certain classes of problems, for instance mixing of two fluids, the interfacial area and local length scales vary with location and time as the mixing process progresses. In this case, tracking the interface between the two fluids can be used to determine the local interfacial area and length scale. Such an algorithm is used in the IFCI code to model the formation of the initial coarse mixture for cases where the size scale of the melt is greater than the finite difference grid size. During this formation phase, as a hot molten fluid mixes with a cold fluid, the characteristic size of the hot fluid changes from values greater than grid cell size to considerably less than grid size. A surface tracking algorithm is used to follow the changes in the geometry of the hot fluid while its characteristic length or diameter is greater than grid cell size. When the hot fluid length scale becomes less than grid size, the hot fluid is assumed to be in a dispersed droplet geometry, and the phenomenological subgrid fragmentation model (Section 3.4.1) is used to determine further changes in length scale.

Surface tracking algorithms based on edge detection, such as SLIC, "Simple Line Interface Calculation," (Noh and Woodward 1976) are not very useful in multifield methods. The difficulty in using such methods is that they are designed for situations where most cells in the problem are either one fluid or the other; the cells containing mixed fluids contain the interface, and the various configurations assumed are based on the adjoining cells being full of a pure fluid. In multifield methods, this situation is reversed: most cells contain both fluids (for a two-field problem) in lesser or greater degree. This is due to the basic design of the multifield method, which allows more than one velocity to exist at the same spatial point. The fields can penetrate one another, controlled by the momentum exchange coefficients and, to some degree, numerical diffusion. For these reasons, an interface tracker based on Volume-of-Fluid methods (Nichols et al. 1980) is more useful for multifield codes.

The surface tracking algorithm is used to account for surface area generated by the distortion of the fuel mass from its initial geometry due to hydrodynamic motion. This is necessary because the fragmentation rate mechanisms [see Equations (3.36) and (3.37)] are both

Basis and Assumptions

subgrid-scale models that do not account for large-scale distortions; they do depend, however, on the characteristic size D . The characteristic size can physically change if, for instance, a fuel mass initially in a single spherical drop distorts into a hollow sphere. The surface tracking algorithm is loosely based on that used in the Volume-Of-Fluid method, except that its primary purpose here is to find the local characteristic diameter, and tracking the interface is a necessary step rather than the final result.

The tracking algorithm is implemented as follows:

1. A sweep of the cells begins in the axial direction starting with the lowest axial level and the innermost radial ring. This sweep first tries to detect the bottom edge of a continuous region of melt. The edge is assumed to be detected when the following criteria are satisfied:
 - (a) The melt cell length scale $D_{j,i}$ is greater than the cell size D_{cell} .
 - (b) The melt volume fraction $\alpha_{j,i}$ is greater than a minimum value, α_{min} (10^{-5} typically).
 - (c) The local change in α must be greater in the axial direction than in the radial direction; that is, the interface must be more horizontal than vertical.
 - (d) The change in melt volume fraction over the cell in the axial direction, $\Delta\alpha$, is greater than or equal to a minimum edge value, α_{edge} . This edge volume fraction change is necessary to prevent small fluctuations in α from yielding a false edge detection, and must be set empirically. Currently, IFCI uses a value of 0.25 to signal an edge. A thorough validation effort might warrant changing this value.
2. If the above criteria are satisfied, then the bottom edge of a melt region is assumed to be at the bottom of the current cell, and the bottom index j_{bot} is assigned the cell bottom edge index, $j-1$. The sweep is continued in the axial direction, with the algorithm now searching for the upper edge of the melt region. The upper edge is signaled if:
 - (a) a horizontal interface is present, as per (1c), and if the axial change in α is negative and greater in magnitude than the edge value:
 $-\Delta\alpha < \Delta\alpha_{\text{edge}}$.

- (b) alternatively, if the melt length scale becomes less than the cell size, signaling a change from a continuous melt region to a dispersed melt region.

The top index j_{top} is then set equal to the top cell index j .

3. When both the upper and lower edges have been detected (or if the upper problem boundary is reached and a bottom edge is present), the melt in the intervening cells is assigned an axial length scale equal to the distance between the top and bottom cells,

$$D_z = z_{j_{\text{top}}} - z_{j_{\text{bot}}} \quad (3.47)$$

The bottom index j_{bot} is then reset, and the sweep continues, again searching for a bottom edge.

4. When the axial sweep is completed, another sweep is started in the next radial ring.
5. Steps 1-4 are repeated until all radial rings have been swept. After completing all axial sweeps, an axial length scale and an interfacial area have been assigned to the melt in each cell of the problem domain.
6. A series of radial sweeps are then started beginning at the bottom axial level in a completely analogous manner to the axial sweeps described above, except that:
 - (a) Vertical surfaces are substituted for horizontal in (1c), and the change of α in the radial direction is computed for comparison with α_{edge} .
 - (b) A radial length scale D_r is computed and averaged with the axial scale from (3) to give a final effective length scale.
 - (c) If the melt is continuous across the axial centerline, then D_r is doubled, so that it represents the diameter rather than the radius.

3.4.3.1 Computation of Slope

The local slope of the interface in a cell is needed to determine whether the interface is more nearly horizontal or vertical. This slope is computed as the cell-size-weighted average of the rate of change of the melt volume fraction α across the two cell edges. The computation is done for both directions. For the axial direction, the derivative is computed as

$$\frac{d\alpha}{dz} = 2 \frac{(\alpha_{j+1,i} - \alpha_{j,i}) \frac{\Delta z_j + \Delta z_{j-1}}{\Delta z_j + \Delta z_{j+1}} + (\alpha_{j,i} - \alpha_{j-1,i}) \frac{\Delta z_j + \Delta z_{j+1}}{\Delta z_j + \Delta z_{j-1}}}{\Delta z_{j-1} + 2\Delta z_j + \Delta z_{j+1}} \quad (3.48)$$

and for the radial direction,

$$\frac{d\alpha}{dr} = 2 \frac{(\alpha_{j,i+1} - \alpha_{j,i}) \frac{\Delta r_i + \Delta r_{i-1}}{\Delta r_i + \Delta r_{i+1}} + (\alpha_{j,i} - \alpha_{j,i-1}) \frac{\Delta r_i + \Delta r_{i+1}}{\Delta r_i + \Delta r_{i-1}}}{\Delta r_{i-1} + 2\Delta r_i + \Delta r_{i+1}} \quad (3.49)$$

IFCI compares the absolute values of the two derivatives and if $d\alpha/dr < d\alpha/dz$, then the interface is more nearly horizontal than vertical, and α is assumed to be a function of z . The change in α across the cell used for comparison with the minimum edge change $\Delta\alpha_{\text{edge}}$ is then computed as

$$\Delta\alpha_z = \frac{d\alpha}{dz} \Delta z_j, \quad \Delta\alpha_r = \frac{d\alpha}{dr} \Delta r_i \quad (3.50)$$

for the axial and radial directions, respectively.

3.4.3.2 Computation of Cell Interfacial Area

The interfacial area of the melt in a cell is computed as the cell flow area times a correction factor which corrects for the tilt of the interface, assuming that the interface can be represented by a straight line in the cell (actually, a conic section, since IFCI 6.0 uses cylindrical geometry).

For purposes of discussion, it is assumed that the interface is more nearly horizontal. With this assumption, the cell-centered axial-flow area for the cell is the average of the top and bottom cell flow areas

$$A = \frac{1}{2} (A_{z_{j,i}} + A_{z_{j-1,i}}) \quad (3.51)$$

The conic section appears as a straight line across the cell if viewed from the side (in the azimuthal direction in r - z -geometry). Since the interface is "horizontal", the continuous melt is assumed to extend across the cell in the radial direction and to fill up the top or bottom of the cell with the interface line forming the boundary. The interface line forms the hypotenuse of a right triangle, with the base being the radial width of the cell r_i and the opposite side being of length Δz_α . The length of the interface line is then given by the equation

$$\Delta s = [\Delta r_i^2 + \Delta z_\alpha^2]^{1/2} \quad (3.52)$$

The ratio of the length of side Δz_α to the cell height Δz_j is equal to the ratio of the change in α between the left and right cell edges (i.e., the difference in magnitude of α between the left and right edges) to the maximum possible α (i.e., 1.0):

$$\frac{\Delta z_\alpha}{\Delta z_j} = \frac{\Delta\alpha_r}{1.0} = \frac{d\alpha}{dr} \Delta r_i \quad (3.53)$$

The interface length can then be written as

$$\Delta s = \Delta r_i \left[1 + \left(\frac{d\alpha}{dr} \Delta z_j \right)^2 \right]^{1/2} \quad (3.54)$$

The term in the square brackets is a constant across the cell, so integrating in the radial and azimuthal direction to get the interface area gives

$$A_s = \overline{A_z} \left[1 + \left(\frac{d\alpha}{dr} \Delta z_j \right)^2 \right]^{1/2} \quad (3.55)$$

where $\overline{A_z}$ is the arithmetic mean of the cell's top and bottom flow areas ("A" in Equation. 3.51). A similar derivation for "vertical" interfaces gives

$$A_s = \overline{A_r} \left[1 + \left(\frac{d\alpha}{dz} \Delta r_i \right)^2 \right]^{1/2} \quad (3.56)$$

where $\overline{A_r}$ is the arithmetic mean of the cell's inner and outer (radial) flow areas.

4. Quality Assurance

Procedures adopted at SNL to assure the quality of the IFCI code can be grouped into three general areas:

- Assessment and validation of individual models and correlations. These procedures apply to both the closure relations for the field equations and the models for specific FCI phenomena, such as dynamic fragmentation.
- Assessment and validation of the complete code against FCI experiments.
- Methods used to assure the code is soundly developed, so as to be reliably useful to the reactor-safety community. Such methods include those used to ensure configuration control, portability and traceability, providing suitable documentation and use of standardized coding practices.

4.1 Models and Correlations

IFCI solves 2D field equations by the SETS method. The hydrodynamics module used (FLUIDS) is described by Dearing (1985) and by Dosanjh (1989). Schmidt et al. (1990) give detailed information on the FLUIDS constitutive relations for water and steam. The additional models of specific importance to IFCI that concern FLUIDS field 4, the melt field, are described in detail in Section 3 of this document. Section 3 also provides an extensive set of references. The following subsections provide additional information on the assessment and validation of the models specific to the melt field.

4.1.1 Stripping Model

The primary stripping model has been validated against small-scale drop breakup data, (Pilch 1981; Marshall and Seebold 1985) and medium-scale melt breakup data. (Young 1987; Young 1990) The results are reasonable, but the data is not prototypical of FCIs. Details are included in Appendix B. The sensitivity of IFCI 6.0 results to this model is not certain. It is a primary subject of a planned validation study.

4.1.2 Flow Regimes

The melt-water-steam flow regime descriptions used by IFCI are theoretically derived, but can be compared to available three-field experimental data. Most of these data describe either non-boiling conditions or the behavior of small drops with phase change in an immiscible fluid.

(Mori 1978) Experimental difficulties have so far precluded observation of actual melt-water-steam flow regimes.

4.1.3 Film Boiling Model

IFCI's film boiling model has been verified for the case of single hot drops surrounded by water. (Dhir and Purohit 1977) An unpublished comparison has been done by M. F. Young at SNL to one- and two-dimensional tests performed at Brookhaven National Laboratory in order to verify that steam production is also correct for large ensembles of drops.

4.2 Comparison of Code Results with Experimental Data

Satisfactory validation of IFCI results against the Sandia FITS experiments has been described by Young (1987, 1990) and Dosanjh (1989). An additional validation effort has been carried out by M. F. Young at SNL using data from the Sandia EJET experiments (Marshall and Beck 1987). The EJET series consisted of five experiments, in which molten iron/alumina in a jet configuration fell into water chambers. Jet diameters ranged from 3.8 cm to 16.3 cm. Davis (see Footnote a from section 1) discusses IFCI 6.0 results for the FITS-D pouring mode experiment, FARO Scoping Test (Joint Research Center 1992), and explosive FCI data from the IET-8 experiments (Allen et al. 1993) performed at Sandia. Preliminary results from IFCI show promising agreement with all the above experimental data.

4.3 Model Limitations

IFCI 6.0 is a stand-alone code, designed to model full-scale FCI accident scenarios. It is intended to model thermal FCIs in as mechanistic manner as possible. IFCI 6.0 does not address chemical energy release, although numerous investigators, including Nelson et al. (1991) and Rightley et al. (1991), have suggested chemical energy may be a real consideration. Model and integrated code validation has not been performed for all possible situations. Important validation gaps include steam explosions in the suppression pool, and reflooding of a degraded core.

Several known limitations exist at this time. The flow regime map requires that the two-dimensional finite difference nodalization be on a sufficiently large scale that the flow regime described is sub-grid scale. Mesh cells

which are too small (on the order of 1 cm for the present flow regime maps) can result in code execution failures, or incorrect results. Errors can occur when the melt contacts cells which are entirely water. This may be avoided by the inclusion of trace quantities of steam in the water phase. This has been discussed in Section 3.4.2. Shortcomings are also present as a result of model limitations. These include the parametric models currently available for the triggering phenomenon and the lack of an oxidation/hydrogen generation model. A validation effort is ongoing which includes addressing and proposing solutions to all of these known limitations.

4.4 Coding Methods

IFCI is written in standard, portable FORTRAN 77. No special system calls are used (library calls are made to LINPACK linear-system solution routines, FORTRAN versions of which are readily available).

The stand-alone version of IFCI, IFCI 6.0, has been developed for use on multiple computer platforms, and has been documented to exist as baseline software. Additional changes will be documented by SNL memoranda. This baseline version has been frozen at the time of the Operational Assessment (see Footnote a from Section 1) which is a companion to this document.

IFCI subroutines (i.e., the melt fragmentation, surface tracking, and area transport routines) have a standard subroutine header, consisting of a set of FORTRAN comments in a standard format based on that in Sandia Software Guidelines, Volume 3, Standards, Practices, and Conventions (1986). This standard header contains the routine's purpose, routines called and called from, and revision history, providing additional traceability.

5. References

- M. A. Abolfadl and T. G. Theofanous, 1987, "An Assessment of Steam-Explosion-Induced Containment Failure. Part II: Premixing Limits," Nucl. Sci. & Eng. 97, pp.282-295.
- M. D. Allen, T. K. Blanchat, M. Pilch, and R. T. Nichols, 1993, "Experiments to Investigate the Effects of Fuel/Coolant Interactions on Direct Containment Heating, The IET-8A and IET-8B Experiments," SAND92-2849, Sandia National Laboratories, Albuquerque, New Mexico.
- S. G. Bankoff and A. Hadid, 1984, "The Application of a User-Friendly Code to Nuclear Thermalhydraulic Reactor Safety Problems," Proc. Int. Nuclear Power Plant Thermal Hydraulics and Operations Topl. Mtg., Taipei, Taiwan, American Nuclear Society.
- R. B. Bird, W. E. Stewart, E. N. Lightfoot, 1960, Transport Phenomena, John Wiley & Sons.
- W. R. Bohl et al., 1987, "Computational Methods of the Advanced Fluid Dynamics Model," Proc. ANS Mtg. on Advances in Reactor Physics, Mathematics, and Computation, Paris, France.
- L. A. Bromley, N. R. LeRoy, and J. A. Robbers, 1953, "Heat Transfer in Forced Convection Film Boiling," Ind. and Engng. Chem., Vol 45, pp.2639-2646.
- C. Carachalios et al., 1983, "A Transient Two-Phase Model to Describe Thermal Detonations Based on Hydrodynamic Fragmentation," Proc. Intl Mtg on LWR Severe Accident Evaluation, Cambridge, MA.
- C. C. Chu and M. L. Corradini, 1989, "One-Dimensional Transient Fluid Model for Fuel/Coolant Interaction Analysis," Nucl. Sci. & Eng. 101, pp.48-71.
- M. L. Corradini, 1981a, "Analysis and Modelling of Steam Explosion Experiments," SAND80-2131, NUREG/CR-2072, Albuquerque, NM.
- M. L. Corradini, 1981b, "Phenomenological Modeling of the Triggering Phase of Small-Scale Steam Explosion Experiments," Nucl. Sci. & Eng. 78, pp.154-170.
- J. F. Dearing, 1985, "A Four-Field Model of PWR Degraded Cores," Third International Topical Meeting on Reactor Thermal-Hydraulics, Newport, RI.
- V. K. Dhir and G. P. Purohit, 1977, "Subcooled Film-Boiling Heat Transfer from Spheres," AICHE-ASME Heat Transfer Conf., Salt Lake City, UT.
- S. S. Dosanjh, 1989, ed., "MELPROG-PWR/MOD1: A Two-Dimensional, Mechanistic Core for Analysis of Reactor Code Melt Progression and Vessel Attack Under Severe Accident Conditions," SAND88-1824, NUREG/CR-5193, Albuquerque, NM.
- D. F. Fletcher and A. Thyagaraja, 1989, "Multiphase Detonation Modelling using the CULDESAC Code," 12th Intl. Colloquium on the Dynamics of Explosions and Reactive Systems, Ann Arbor, MI.
- G. A. Greene, T. Ginsberg, N. K. Tutu, 1985, "BNL Severe Accident Sequence Experiments and Analysis Program," Proc. Twelfth Water Reactor Safety Research Information Mtg., NUREG/CP-0058, 3.
- T. J. Heames, 1989, "MELPROG PWR/MOD1 User's Manual", SAND90-0597.
- M. Ishii, 1975, Thermo-Fluid Dynamic Theory of Two-Phase Flow, Eyrolles, France.
- R. P. Jenks and V. Martinez, 1988, "TRAC Support Software," NUREG/CR-5071, Los Alamos National Laboratory, June 1988.
- Joint Research Center, 1992, "FARO LWR Programme : Scoping Test Data Report," Technical Note No. I.92.135, Institute for Safety Technology, Ispra, Italy.
- J. E. Kelly, 1985, "MELPROG: An Integrated Model for In-Vessel Melt Progression Analysis," Thirteenth Water Reactor Safety Research Information Meeting, Gaithersburg, MD.
- B. Kim, 1985, "Heat Transfer and Fluid Flow Aspects of Small-Scale Single Droplet Fuel-Coolant Interactions," Ph. D. dissertation, University of Wisconsin, Madison, WI.
- B. Kim and M. L. Corradini, 1988, "Modeling of Small-Scale Single Droplet Fuel/Coolant Interactions," Nucl. Sci. & Eng. 98, pp.16-28.
- G. Kocamustafaogullari, 1971, "Thermo-Fluid Dynamics of Separated Two-Phase Flow," Ph. D. dissertation, Georgia Inst. of Technology, Atlanta, GA.
- K. Lee and D. J. Ryley, 1968, "The Evaporation of Water Droplets in Superheated Steam," ASME 68-HT-11.

- D. R. Liles et al., 1988, "TRAC-PF1/MOD1 Correlations and Models," LA-11208-MS, NUREG/CR-5069, Los Alamos, NM.
- Los Alamos Safety Code Development Group, 1986, "TRAC- PF1/MOD1: An Advanced Best-Estimate Computer Program for Pressurized Water Reactor Thermal-Hydraulic Analysis," Los Alamos National Laboratory report LA-10157-MS NUREG/CR- 3858.
- J. H. Mahaffy, 1982, "A Stability-Enhancing Two-Step Method for Fluid Flow Calculations," J. Comp. Phys. 46, p.329.
- B. W. Marshall, Jr.,1988, "Recent Fuel-Coolant Interaction Experiments Conducted in the FITS Vessel," 25th ASME/AIChE National Heat Transfer Conference, Houston, TX.
- B. W. Marshall, Jr. and D. F. Beck, 1987, "The Coarse Mixing of Boiling and Isothermal Jets," SAND87-2455C.
- B. W. Marshall, Jr. and O. P. Seebold, 1985, "Reactor Safety Research Semiannual Report January-June 1985," 33, SAND85-1606, pp. 67-71, Albuquerque, NM.
- S. Medhekar et al., 1988, "Triggering and Propagation of Steam Explosions," 25th ASME-AIChE Heat Transfer Conference, Houston, TX.
- B. B. Mikic et al., 1970, "On Bubble Growth Rates," Int. J. Heat Mass Transfer 13, pp.657-666.
- D. E. Mitchell et al., 1981, "Intermediate Scale Steam Explosion Phenomena: Experiments and Analysis," SAND81- 0124, NUREG/CR-2145, Albuquerque, NM.
- Y. H. Mori, 1978, "Configurations of Gas-Liquid Two-Phase Bubbles in Immiscible Liquid Media," Int. J. Multiphase Flow, 4.
- L. S. Nelson, P. M. Duda, and D. A. Hyndman, 1991, "Interactions Between Drops of Molten Al-Li Alloys and Liquid Water," SAND91-2191.
- B. D. Nichols et al., 1980, "SOLA-VOF: A Solution Algorithm for Transient Fluid Flow with Multiple Free Boundaries," LA-8355, Los Alamos, NM.
- H. C. No and M. S. Kazimi, 1985, "Effect of Virtual Mass Effects on the Mathematical Characteristics and Numerical Stability of the Two-Fluid Model", Nucl. Sci. & Eng. 89, pp.197-206.
- W. F. Noh and P. Woodward, 1976, "SLIC (Simple Line Interface Calculation)," Proceedings of the Fifth International Conference on Numerical Methods in Fluid Dynamics, A.I. van de Vooren and P. J. Zandbergen, eds., Springer-Verlag (Lecture Notes in Physics, 59).
- M. Pilch, 1981, "Acceleration Induced Fragmentation of Liquid Drops," Ph. D. dissertation, University of Virginia, Charlottesville, VA.
- M. J. Rightley, D. F. Beck, and M. Berman, 1991, "NPR/FCI EXO-FITS Experiment Series Report," SAND91-1544.
- P. J. Roache, 1972, Computational Fluid Dynamics, Hermosa Publishers, Albuquerque, NM.
- "Sandia Software Guidelines, Volume 3, Standards, Practices, and Conventions," 1986, SAND85-2346, Albuquerque, NM.
- R. C. Schmidt et al., 1990, "MELPROG PWR/MOD1 Models and Correlations," SAND89-3123, NUREG/CR-5569, Albuquerque, NM.
- M. G. Stevenson, 1980, "Report of the Zion/Indian Point Study," Los Alamos National Laboratory report LA-8306-MS, NUREG/CR-1411, Los Alamos, NM.
- D. V. Swenson and M. L. Corradini, 1981, "Monte Carlo Analysis of LWR Steam Explosions," SAND81-1092, NUREG/CR- 2307, Albuquerque, NM.
- A. Thyagaraja and D. F. Fletcher, 1986, "Buoyancy-Driven, Transient, Two-Dimensional Thermo-Hydrodynamics of a Melt- Water-Steam Mixture," CLM-P790, UKAEA, Culham Laboratory, Abingdon, UK.
- M. F. Young et al., 1979, "The FCI Potential of Oxide and Carbide Fuels: Results of the Prompt Burst Series at Sandia Laboratories," Fourth CSNI Specialist Meeting on Fuel-Coolant Interaction in Nuclear Reactor Safety, Bournemouth, UK.
- M. F. Young, 1982, "The TEXAS Code for Fuel-Coolant Interaction Analysis," Proceedings of the LMFBR Safety Topical Meeting, Lyon-Ecully, France.
- M. F. Young, 1987, "IFCI: An Integrated Code for Calculation of All Phases of Fuel-Coolant Interactions," Sandia National Laboratories report SAND87-1048, NUREG/CR- 5084, Albuquerque, NM.

References

- M. F. Young, 1990, "Application of the IFCI Integrated Fuel-Coolant Interaction Code to a FITS-Type Pouring Mode Experiment, "Dynamics of Detonations and Explosions : Explosion Phenomena, AIAA, Vol 134.

6. Appendix A : Input Description

IFCI Version 6.0h

INTRODUCTION

IFCI is derived from the FLUIDS module of the MELPROG/MOD1 severe accident analysis code. As such, the input format is basically the same as that for MELPROG FLUIDS with some extensions for the FCI models in IFCI. Only a few of the input variables have been removed from the MELPROG version of IFCI prior to completion of code assessment. However, a number of calculations are no longer performed when using the stand alone version of the code. Additional parameters may be deleted upon completion of the Operational Assessment and Peer Review.

INPUT DESCRIPTION

IFCI can be run in two modes - an initialization mode or a restart mode. In both modes the necessary input will be read from unit 95, but this file will be substantially smaller during the restart mode because most of the information will be obtained from the restart file (written to unit 98, and read in as unit 93). In the following sections, the initialization input file and the restart input file are described.

GENERAL ORGANIZATION

An IFCI input deck is organized by module and contains the data necessary for problem control as well as fluids, materials, geometry, initial and boundary conditions. These data are contained in unit 95 and must be in a specified order.

The problem control data input consists of general parameters such as titles, restart and dump information, beginning and ending time, maximum time step, and convergence criteria. This data must always be present in unit 95. The module input consists of the information necessary to specify and control the problem within each module.

FREE FORMAT INPUT STRUCTURE

The data are read into the code using a free format input processor, FUNRD[1]. With this processor the order in which numbers are read is determined by the code and therefore a card out of order will cause an error. This input processor does not allow for default values, i.e., all required inputs must be entered. Values in the input description which are offset with parentheses are typical values. The typical values may be used in the absence of additional information.

DATA. Data is acceptable as integer, fixed field, or scientific notation. In the latter case, "e" is used to indicate the exponent field. All of the following values will be interpreted equivalently (100 100.0 1.0e2 1.0e+2).

SEPARATORS. Data is delimited by a comma (,) or a space () or the end of the record (column 80).

REPETITION. Repetition of values may be done with the form "n*v", where n is the number of times the value v is to be read. Repetition of groups of values is done with the form "n*(m1*v1, m2*v2, ...)", where n is the number of times the group within the parentheses is repeated. The total number of values that can be read on one line is 40; therefore something like "60*0.05" must be broken up into "40*0.05" on one line and "20*0.05" on the following line. Note: there can not be any separation between the number of values, n, and the asterisk, *, as this will cause the input data to be incorrectly interpreted as successive values.

CONTINUATIONS. Successive values are assumed to be either on the same card or on the next non-comment card, therefore the user may use 1 card to input 5 values or as many as 5 cards.

EXCESS DATA. Additional data on cards is ignored. In the detailed input description that follows each read statement has been given a number. The user cannot connect read statements, for example the second read is the restart flag, IRESTRT. Any additional numbers on the card will be flagged by the code as a possible error and ignored.

COMMENT CARDS. A \$ in column 1 identifies the card as a comment card. The card will only be printed as read. There is no limit to the number or location of these cards.

UNITS. S.I. units are used for all IFCI input, as shown in Table A-1.

TABLE DATA. IFCI inputs table data in (x,y) pairs, for example (time, power level) or (time, exit pressure). The code linearly interpolates between points in the table, uses a constant value beyond table limits, and requires a minimum of two table pairs. It should be noted that no warnings are printed for values beyond table limits.

ARRAY DATA. IFCI inputs array data, for example the cell by cell additive friction factors, according to standard FORTRAN rules. This means that the friction factors are input as consecutive axial nodes, from bottom to top, for each radial ring, starting from the innermost ring.

Table A.1. S.I. Units Used For IFCI.

Quantity	S.I. Unit	Quantity	S.I. Unit
Length	m	Density	kg/m ³
Mass	kg	Time	s
Volume	m ³	Power	W
Temperature	K	Pressure	Pa
Velocity	m/s	Viscosity	Pa-s
Surface Tension	kg/s ²	Torque	N-m
Specific Heat	J/kg-K	Thermal Conductivity	W/m-K
Heat Transfer Coefficient	W/m ² -K	Volumetric Heat Source	W/m ³

PROBLEM INITIALIZATION (unit 95)

In the following detailed IFCI input specifications each READ statement has been given a number, therefore READ statement number 3 is expecting values for DMPINT, GFINT, and EDITN. These values are placed on separate lines or on the same line. After enough lines have been read to yield 3 input values, IFCI will proceed to read statement 4 input beginning with the next line. Any additional information remaining on the current line will be ignored.

GENERAL INPUT

1. ITITLE (20A4)
 - A. ITITLE = problem title (up to 80 characters)
2. IRESTRT
 - A. IRESTRT = the restart switch, set to 0 for initialization
3. DMPINT, GFINT, EDINT
 - A. DMPINT = Restart dump interval (sec) (unit 98; this file contains the information necessary to restart the code at the end of this interval).
 - B. GFINT = Graphics dump interval (sec) (unit 92; this file contains graphics information)
 - C. EDINT = Full edit interval (sec) (unit 96; this file contains the printed output)
4. PRNTTO
 - A. PRNTTO = Problem time or step number at which an additional full edit is desired. The logic within the code is such that an input value of 12 would yield a full print at both the 12th step and at 12 seconds. Typically this input is set to a large value or used to examine the calculation at a known time, for example, failure in an experiment.
5. IPRTF, IPRTR, IPRTD
 - A. IPRTF = FLUIDS module full print flag (0=off, 1=field data, 2=transfer function data, 3=fluid property data).
 - B. IPRTR = RADIATION module full print flag (0=off, 1=on)
 - C. IPRTD = DEBRIS module full print flag (0=off, 1=on).

NOTE: The values chosen for these flags only controls the amount of output sent to unit 96. If verifying the input set these flags to their maximum value, if the code is experiencing problems set IPRTF=2.
6. KMAX, NRING
 - A. KMAX = Number of axial nodes.
 - B. NRING = Number of radial rings.

NOTE: The values chosen for KMAX and NRING determine to a large part the total computational time the problem will take.

NOTE: The total number of cells allowed, KMAX*NRING, is controlled by the length of two container arrays within the code, X and XLCM. After the input has been read, the code will determine the total length for these arrays and whether the user has exceeded the compiled limits. At this time, IFCI does not have a dynamic allocation system capable of making the correct adjustments to these arrays, hence if the user finds that they have exceeded the current limits they must recompile the main driver routine, RMPPROG, with the necessary changes.
7. GASCOEF
 - A. GASCOEF = Maximum fraction of the vapor internal energy that the vapor can receive from all heat sources in one time step. This variable will control the time step in many cases (typical values range from 0.05 when the vapor is hot to 0.25 when it is cold).
8. TIME, ENDTIM, DELTO
 - A. TIME = The starting time (sec).
 - B. ENDTIM = Problem end time (sec).
 - C. DELTO = The initial time step (sec). Typically we initially use a small step and allow the code to control the increases. (0.05)
9. NTIM
 - A. NTIM = Number of time step pairs in the maximum allowable IFCI time step table (> 1).
10. STEP(l,n), l=1,2 n=1,NTIM

- A. STEP = Maximum allowable time step table, NTIM pairs of problem time (seconds) and maximum time step (seconds) Typically, values between 0.25-1.0 are used for the maximum time step. If the code has time step control problems associated with the explicit links between modules the user can lower this value to control the calculation.

FLUID DYNAMICS MODULE INPUT

In this section of the input the user will supply most of the data necessary to describe the problem from the FLUIDS point-of-view.

Fluids Module Input: Scalar Data

11. DTINC
 - A. DTINC = Maximum allowable fractional time step increase between steps.
(typical value is 1.05)
 12. DTMIN
 - A. DTMIN = Minimum time step. If the code requires a step size below this value the problem terminates. (sec) (typical value is 1.0e-9)
 13. CRFAC
 - A. CRFAC = Courant multiplication factor. This determines a time step due to the fluid Courant condition (mesh size/velocity) times CRFAC. If too large, fluid temperature oscillations will occur (typical values are 1-10).
 14. ITERMIN, ITERMAX
 - A. ITERMIN = Minimum iterations. The time step may only increase if the number of pressure iterations taken in the FLUIDS module is less than ITERMIN. (typical values are 3-5).
 - B. ITERMAX = Maximum number of pressure iterations that can be taken in the FLUIDS module before failure. If the error has been decreasing during the iteration but is still larger than ERROR1, when ITERMAX is reached, the code will print a warning and accept the calculation. If the error is not decreasing, the time step is reduced by 10% and an explicit calculation is executed. (typical values are 10-20).
 15. ERROR1
 - A. ERROR1 = Error criterion 1 for the Newton-Raphson iteration. This is the convergence criterion on the change in relative pressure from iteration to iteration in the FLUIDS calculation. The change in pressure from iteration to iteration may not always force the necessary convergence of the velocities and temperatures, therefore we recommend a tight convergence (typical values are 1.0e-9 - 2.0e-5).
 16. EPSA
 - A. EPSA = Maximum fractional change in fluid volume fraction between time steps. (typical values are 0.1-0.5)
 17. EPST
 - A. EPST = Maximum fractional change in fluid temperature between time steps (typical values are 0.01-0.1).
 18. CONDCOE
 - A. CONDCOE = Coefficient multiplying the bulk condensation rate (1.0e-4).
- NOTE: DCOR3 and DCOR4 are used for the corium-water and melt-water interaction models and small values will force a significant evaporation rate to occur.
19. DCOR3
 - A. DCOR3 = Diameter of the particles represented in field 3, solid corium. (m).
 20. DCOR4

- A. DCOR4 = Initial characteristic diameter of the molten material in field 4, liquid corium. (m) (typical values are 0.02-0.04)
21. MATID3(l), l=1,8
- A. MATID3 = Pattern of material identifiers to be used for field 3 and field 4 corium properties. If eight 0's are entered the default pattern of 1,17,3,4,5,6,13,14 or (UO₂, Ag-In-Cd, Zr, ZrO₂, SS, SSOx, INC, INCOx) is used. A value for the total number of materials being considered, ICMPIN, is determined by finding the first 0 in the data. When deciding upon a pattern for MATID3 the user should be aware that the oxidation routines assume that the base metal will be followed in the pattern by the oxide, for example Zr by ZrO₂. The current 1-dimensional DEBRIS module separates materials 1, 17, 3, and 4 and lumps all others into 5 (stainless steel), this lumping may cause incorrect answers. Most combinations of materials are mixed to determine an average property in accordance with their masses, however the combination of UO₂-Zr-ZrO₂ uses a phase diagram. All the materials in subroutine MATPRO are available as corium material mixtures and their identifying numbers are:
- a) MATID3 = 1, UO₂ (Urania).
 - b) MATID3 = 2, UO₂-PuO₂ mixture.
 - c) MATID3 = 3, Zircaloy 4.
 - d) MATID3 = 4, ZrO₂ (zirconia).
 - e) MATID3 = 5, stainless steel type 304.
 - f) MATID3 = 6, steel oxide mixture FeO-Cr₂O₃ (Iron chromate).
 - g) MATID3 = 7, stainless steel type 316.
 - h) MATID3 = 11, Medium carbon steel type A.
 - i) MATID3 = 13, Inconel 718.
 - j) MATID3 = 15, Inconel 600.
 - k) MATID3 = 17, Ag-In-Cd control rod material.
 - l) MATID3 = 19, B₄C control rod material.
 - m) MATID3 = 20, Aluminum metal
 - n) MATID3 = 21, Al₂O₃ Aluminum oxide.
 - o) MATID3 = 22, Stoichiometric Fe-Al₂O₃ Thermite.
 - p) MATID3 = 24, Fe Iron metal, liquid primarily.
 - q) MATID3 = 25, FeO Iron oxide, Wustite.
 - r) MATID3 = 26, ZrO₂, 91% pure Zirc oxide ceramic, shroud material.
 - s) MATID3 = 27, ZrO₂ fiber, 79% porous, steam filled, shroud material.
 - t) MATID3 = 28, ZrO₂ fiber, 79% porous, water filled, shroud material.
 - u) MATID3 = 29, ZrO₂ fiber, 79% porous, water-steam filled shroud material.
22. FRAC34(l), l=1,8
- A. FRAC34 = Reference mass fractions for fields 3 and 4. These are the initial mass fractions corresponding to the material id's entered above (MATID3). The solid/liquid corium equation-of-state (EOS) uses these reference values to determine mass-weighted properties, such as density or heat capacity.
23. PREF
- A. PREF = Reference pressure for fields 3 and 4. The corium thermodynamic EOS uses this parameter (Pa) (see IFCI MODELS AND CORRELATIONS document for the form of the EOS).
24. TREF3, TREF4
- A. TREF3 = Reference temperature for field 3. The solid corium caloric and thermodynamic EOS's use this parameter. (K)
- B. TREF4 = Reference temperature for field 4. Same as above for liquid corium EOS. (K)
25. ASQ3, ASQ4
- A. ASQ3 = Inverse sound speed squared for field 3. The solid corium thermodynamic EOS uses this parameter. (s²/m²)
- B. ASQ4 = Inverse sound speed squared for field 4. The liquid corium thermodynamic EOS uses this parameter. (s²/m²)
26. IDETFLG, IDETTRG, IFRAG
- A. IDETFLG = Flag to turn detonation models on or off. 0 = off, 1 = on.

- B. IDETTRG = Detonation trigger/model selector. This selects one of the trigger models and associated detonation model:
1. 0 = Pure parametric model, detonation is triggered in cell (JTRG, ITRG) at time TIMTRG (see model- specific input below).
 2. 1 = Pressure threshold model, detonation is triggered when pressure in a cell exceeds a trigger pressure threshold.
 3. 2 = Pressure/pressure rise rate threshold model, detonation triggers when pressure and pressure rise rate both exceed threshold levels.
- C. IFRAG = Flag to turn fragmentation models on or off. 0 = off, 1 = on.

THE FOLLOWING LINE IS MODEL-SPECIFIC

27. *for IDETTRG = 0:*
JTRG, ITRG, TIMTRG
- A. JTRG = Axial level number for trigger cell.
- B. ITRG = Radial ring number for trigger cell.
- C. TIMTRG = Time at which to trigger (s).
28. *for IDETTRG = 1:*
PTRG
- A. PTRG = Pressure threshold (Pa).
29. *for IDETTRG = 2:*
PTRG, PTRGRAT:
- A. PTRG = Pressure threshold (Pa).
- B. PTRGRAT = Pressure rise rate threshold (Pa/s).
30. DFRAG, TAUFRAG, IHTDET, HTDET
- A. DFRAG = Fine fragment diameter (m).
- B. TAUFRAG = Fine fragmentation time (s).
- C. IHTDET = Fine fragment heat transfer flag, 0 = use standard correlations, 1 = use input parameter HTDET for heat transfer to fine fragments.
- D. HTDET = Fine fragment heat transfer coefficient (W/m²).
31. ITPTS, IIOUT
- A. ITPTS = Number of steps between short FLUIDS prints. (1 line will be printed to standard output and to unit 96).
- B. IIOUT = For your information print control; a user determined value will be edited on short FLUIDS print. A value of IIOUT =:
1. 0 =Consecutive edit of all of the values below. (this is the recommended input).
 2. 1 =Values of the FLUIDS knobs. A five digit number consisting of 0's and 1's, with a 0 indicating that a fluid field is off and a 1 is on. The fields are steam, water, solid corium, liquid corium, and hydrogen. (10001. = all vapor mixture of steam and hydrogen)
 3. 2 =Total hydrogen generation rate (kg/s).
 4. 3 =Maximum cladding temperature (K).
 5. 4 =Maximum heat transfer coefficient between a rod and vapor (W/m²-K).
 6. 5 =Maximum power generation due to oxidation (W/m³).
 7. 6 =Maximum power transferred to either the vapor or the water fields (W/m³).
 8. 7 =Maximum net heat flow between water and vapor (W/m³).
 9. 8 =Maximum pressure in vessel (Pa).
 10. 9 =Liquid temperature exiting the vessel (K).
 11. 10 =Vapor temperature exiting the vessel (K).
 12. 11 =Total steam generation rate (kg/s).
 13. 12 =Volume of liquid water in vessel (m³).
 14. 13 =Total mass divergence, a measure of the conservation of mass within the FLUIDS calculation. (kg).

Fluids Module Input: Array Data

NOTE: The additive friction factors for each field (vapor, liquid, solid corium, liquid corium) have the following uses:

- (1) To allow or prevent flow between adjacent cells (input 0.0 and $> 1.0\text{e}20$ respectively). This enables the user to model internal structures, which are not explicitly modeled, but may restrict axial, or radial, flow.
- (2) To throttle the flow to get the correct cell to cell flow velocities at steady conditions. The FLUIDS module uses cell edge velocities and cell centered pressures, the additive friction factor is: pressure drop / (avg cell height/hydraulic diam) / kinetic energy, where $k.e. = (0.5 * \rho * v * \text{abs}(v))$. Typical values for velocities and pressure drops come from either other codes or experimental measurements.

32. NADR

- A. NADR = Number of regions for additive friction factors. Each region will be bounded by ILFT, JBOT, IRIGHT, and JTOP.

NOTE: The following boundaries and axial/radial friction factors are input as a group (lines 33-41) NADR times, one group for each region.

33. ILFT, JBOT, IRIGHT, JTOP

- A. ILFT = Ring number of first cell on left boundary of region.
 B. JBOT = Axial node number of lowest cell in region.
 C. IRIGHT = Ring number of last cell on right boundary of region.
 D. JTOP = Axial node number of highest cell in region.

NOTE: The radial direction is described by rings, or cells, e.g., RING 1 is bounded by the first radial node (at 0.0) on the interior, and the second radial node on the exterior or right hand side. The axial direction is described by the axial nodes.

34. ADKZ(j,i), j=JBOT,JTOP i=ILFT,IRIGHT

- A. ADKZ = Additive axial friction factor applied at top of axial node J in ring I for field 1, vapor.

35. ADKZ(j,i), j=JBOT,JTOP i=ILFT,IRIGHT

- A. ADKZ = Additive axial friction factor applied at top of axial node J in ring I for field 2, water.

36. ADKZ(j,i), j=JBOT,JTOP i=ILFT,IRIGHT

- A. ADKZ = Additive axial friction factor applied at top of axial node J in ring I for field 3, solid corium. Corium is typically able to melt through most materials and a value $> 1.0\text{e}20$ will prevent it from falling correctly.

37. ADKZ(j,i), j=JBOT,JTOP i=ILFT,IRIGHT

- A. ADKZ = Additive axial friction factor applied at top of axial node J in ring I for field 4, liquid corium.

38. ADKR(j,i), j=JBOT,JTOP i=ILFT,IRIGHT

- A. ADKR = Additive radial friction factor applied at right hand face of axial node J in ring I for field 1, vapor.

39. ADKR(j,i), j=JBOT,JTOP i=ILFT,IRIGHT

- A. ADKR = Additive radial friction factor applied at right hand face of axial node J in ring I for field 2, water.

40. ADKR(j,i), j=JBOT,JTOP i=ILFT,IRIGHT

- A. ADKR = Additive radial friction factor applied at right hand face of axial node J in ring I for field 3, solid corium. We assume that walls can inhibit the radial flow of corium.

41. ADKR(j,i), j=JBOT,JTOP i=ILFT,IRIGHT

- A. ADKR = Additive radial friction factor applied at right hand face of axial node J in ring I for field 4, liquid corium.

Fluids Module Input: Boundary Conditions

NOTE: The code assumes that no fluid field can either enter or exit the problem domain (the outer ring and the bottom and top axial nodes). To allow inflow and outflow to the problem domain, the following input is needed. The current version of the code only allows inflow and outflow at the outer boundaries.

42. NINBC
A. NINBC = Number of cell locations used for inflow boundary conditions
(NINBC must be <6).

NOTE: The following inflow boundary condition parameters are repeated as a group (lines 43-55) NINBC times, one group for each inflow location.

43. INN
A. INN = For either a top or bottom inflow boundary condition, INN is the radial ring number whose lower interface coincides with the inflow boundary, $1 \leq \text{INN} \leq \text{NRING}$. For an inflow boundary on the right face, $\text{INN} = \text{NRING} + 1$.
44. JIN
A. JIN = For a right boundary condition, JIN is the axial node number whose outer interface coincides with the inflow boundary, $1 \leq \text{JIN} \leq \text{KMAX}$. For a top boundary condition, this will be $\text{KMAX} + 1$. For a bottom boundary condition, $\text{JIN} = 0$.
45. ARIN
A. ARIN = Flow area at the inflow boundary (m^2). Typically a mass flow is known and this input is used to relate the known flow to the inlet tables below.
46. NPRIN
A. NPRIN = Number of entries in inflow pressure condition tables (< 100).
47. NVIN
A. NVIN = Number of entries in inflow boundary condition velocity tables (< 100).
48. NTIN
A. NTIN = Number of entries in inflow boundary condition temperature tables (< 100).
49. NAIN
A. NAIN = Number of entries in inflow boundary condition volume fraction tables (< 100).

NOTE: The inflow pressure tables are only used to determine the physical properties of the incoming fluid and not the pressure in the problem.

50. PRNTAB(l,n), l=1,2 n=1,NPRIN
A. PRNTAB = Inflow total pressure table, NPRIN pairs of time (sec) and pressure (Pa).
51. PH2TAB(l,n), l=1,2 n=1,NPRIN
A. PH2TAB = Inflow hydrogen partial pressure table, NPRIN pairs of time (sec) and pressure (Pa). Must be less than the values in PRNTAB except in the case of a pure noncondensable, in which case $\text{PH2TAB} = \text{PRNTAB}$.

NOTE: The following velocity, temperature, and volume fraction inflow tables (lines 52-54) are input as a group for each of the 4 inflow fields. The mass fractions (line 55) are also input if fields 3 or 4 are in the inflow.

52. VINTAB(l,n), l=1,2 n=1,NVIN
A. VINTAB = Inflow boundary condition velocity table for a field, NVIN pairs of time (sec) and velocity (m/s). Positive velocity direction is from the bottom to the top and from the centerline to the radial boundary. This means that an inflow on a radial boundary has negative values for velocity.

53. TINTAB(l,n), l=1,2 n=1,NTIN
 A. TINTAB = Inflow boundary condition temperature table for a field, NTIN pairs of time (sec) and temperature (K).
54. AINTAB(l,n), l=1,2 n=1,NAIN
 A. AINTAB = Inflow boundary condition volume fraction table for a field, NAIN pairs of time (sec) and fraction. The sum of the volume fractions for all fields should be unity.
55. FRC34(m,k), m=1,8 k=3,4
 A. FRC34 = Mass fractions of the inflow eutectics. Input mass fraction is input for both fields 3 and 4 if the volume fraction for either field 3 or 4 indicates their presence. If neither field 3 or field 4 will be in the inflow, this input is not read.

****Begin outflow pressure boundary condition section, this pressure is used to determine the pressure within the problem.

56. NPBC
 A. NPBC = Number of locations for outlet pressure boundary condition's (<6)

Note: The following outflow boundary condition parameters, are repeated as a group (lines 57-62) NPBC times, one group for each outflow location.

57. MPBC
 A. MPBC = Boundary condition location flag (outer radial = 1, top axial =2).
58. MOUT
 A. MOUT = Axial node for radial outflow pressure boundary condition, if MPBC=1. Radial ring for axial outflow pressure boundary condition, if MPBC=2. This is always on the outside of the mesh, so if MPBC=1 then $1 \leq MOUT \leq KMAX$, and if MPBC=2 then $1 \leq MOUT \leq NRING$. Note that having an inflow and an outflow on the right face of the same cell will cause unrealistic answers.
59. AROUT
 A. AROUT = Outflow area (m^2).
60. HDOUT
 A. HDOUT = Outflow hydraulic diameter (m).
61. NPROUT
 A. NPROUT = Number of entries in outflow pressure boundary condition table (< 100).
62. PROTAB(l,n), l=1,2 n=1,NPROUT
 A. PROTAB = Outflow pressure boundary condition table, NPROUT pairs of time (sec) and pressure (Pa).

Fluids Module Input: Initial Conditions

NOTE: The following input initializes the problem domain in terms of pressure, temperature, velocities, volume fraction, and mass fraction. The values are input as constants over a region, variations in pressure across region boundaries are difficult for the code unless the additive friction at the boundary is sufficient.

63. NRGIN
 A. NRGIN = Number of regions for initial conditions, must initialize problem domain.

NOTE: The following region boundaries and initial conditions are input as a group (lines 64-71) NRGIN times, one group for each region.

64. ILFT, JBOT, IRIGHT, JTOP
 A. ILFT = Ring number of first cell on left boundary of region.
 B. JBOT = Axial node number of lowest cell in region.
 C. IRIGHT = Ring number of last cell on right boundary of region.

65. D. JTOP = Axial node number of highest cell in region.
 PIN, PINH2
 A. PIN = Total pressure in the region.(spatially uniform) (Pa).
 B. PINH2 = Hydrogen partial pressure in the region. (Pa).
66. ALIN(k), k=1,4
 A. ALIN = Initial fluid volume fraction for field K. The sum of the four fluid volume fractions should be 1.0.
67. FRAC3(m), m=1,8
 A. FRAC3 = Initial eutectic mass fractions in the region for field 3, input only if ALIN(3) > 0. The input pattern is the same as used in the inflow boundary conditions for fields 3 and 4. The default pattern is UO₂, AIC, Zr, ZrO₂, SS, SSO_x, INC, INCO_x.
68. FRAC4(m), m=1,8
 A. FRAC4 = Initial eutectic mass fractions for field 4, input only if ALIN(4) > 0. Input pattern is the same as FRAC3(m) comments.
69. TIN(k), k=1,4
 A. TIN = Initial temperature in the region for field k (K).
70. VIN(k), k=1,4
 A. VIN = Initial axial velocity (spatially uniform) in the region for field k (m/s).
71. VRIN(k), k=1,4
 A. VRIN = Initial radial velocity (spatially uniform) in the region for field k (m/s). This value is typically much smaller than VIN.
72. AL10
 A. AL10 = Low volume fraction limit for all fields. If the volume fraction of a fluid field is calculated to be below this value, the FLUIDS calculation (mass, energy, and momentum) for that field is turned off for the next time step. (1.0e-8 - 1.0e-5, function of whether the case has a low (0.1MPa) or high (10.0MPa) pressure respectively).

Fluid Module Input: Geometry Data

73. DZ(j), j=1,KMAX
 A. DZ = Length of each axial node (m). Avoid order of magnitude changes from node to node. Attempt to place the midpoint of nodes near known thermocouple junctions. If a critical phenomenon is anticipated to happen at a particular location, add an extra cell to help define it better.
74. RA(i), i=1,NRING+1
 A. RA = Radial position of rings (m). Note that there are NRING+1 of these, starting at RA(1)=0 and going to outer edge of problem.

NOTE: Embedded passages allow the transmission of steam and water between any two cells within a ring while skipping all intermediate cells. These are typically used to describe the flow through passages.

75. IMBED
 A. IMBED = Number of embedded passages
- NOTE: If IMBED > 0, the following is input as a group IMBED times.
76. NRIMB
 A. NRIMB = Radial ring number for embedded passage.
77. NZTIMB, NZBIMB
 A. NZTIMB = Axial node number of cell at upper interface of the embedded passage.
 B. NZBIMB = Axial node number of cell at lower interface of the embedded passage.
78. FAZIMB
 A. FAZIMB = Flow area of embedded passage (m²).

79. ADKIMB
 A. ADKIMB = Friction factor of embedded passage.

INPUT UNUSED BELOW THIS POINT

STRUCTURES MODULE INPUT

The STRUCTURES module input was used describe all structure, and place them on the computational mesh. No longer used, so use defaults suggested below.

Structures Module Input: Scalar Data

80. MAXMOD, STCNVG, SFCNVG, ITCRST, ITMELT
 A. MAXMOD = Number of unique structure models to be input. If set = 0, no structure heat transfer nor stress analysis calculation and no additional input is required beyond the 5 values indicated on this card.
 B. STCNVG = Freezing and melting convergence criterion.
 C. SFCNVG = Crust freezing and melting convergence criterion.
 D. ITCRST = Maximum iterations on crust.
 E. ITMELT = Maximum iterations on structure melting.

Suggested values: 0 0.1 0.1 5 5

RADIATION HEAT TRANSFER MODULE INPUT

The Radiation module input allows the user to control the radiation heat transfer calculation.

81. NGROUP
 A. NGROUP = Number of radiation groups (1)
 82. ITRMAX
 A. ITRMAX = Max number of iterations. (50, for FLUID axial cell heights substantially larger than the radius, 100 or more if they become more comparable in size)
 83. RCONV
 A. RCONV = Radiation convergence criterion. (1.0e-4, if this error is exceeded by an order of magnitude then ITRMAX should be increased)
 84. TBOUND
 A. TBOUND = Radiation boundary sink temperature (300 K).
 85. EMISS(k), k=1,6
 A. EMISS = Emissivity of structure K. The structures are: rods, outer wall, inner wall, bottom plate, top plate, and debris. (We typically use a value of 0.3 for the solid structures and 0.8 for the debris bed)
 86. RFAC, ARHOL, ARHOC, ARHOM
 A. RFAC = Planck mean absorption coefficient multiplier for steam. (1.0) Subprogram FKPM provides the value for the coefficient as a function of pressure and temperature, RFAC allows the user to adjust the level.
 B. ARHOL = Liquid absorption coefficient. (a typical range is 0.05-0.10)
 C. ARHOC = Solid corium absorption coefficient. (0.1, assumes an oxidized surface and high temperatures)
 D. ARHOM = Liquid corium absorption coefficient. (0.1)

DEBRIS MODULE INPUT

The DEBRIS module input allows the user to control the model through the formation, meltdown, and existence of the calculation.

87. LDBRIS
 A. LDBRIS = DEBRIS module calculation switch. (0=off, 1=on) (0)
88. NZMAX, NBEDM, ICOND
 A. NZMAX = Maximum number of nodes in a bed (40-60).
 B. NBEDM = Maximum number of beds (1).
 C. ICOND = Effective conductivity model indicator (1).
 1. ICOND = 1, The Imura-Takegoshi/Vortmeyer model is used.
 2. ICOND = 2, The Willhite-Kunii-Smith/Luikov model is used.
89. ALFDBM, PORMAX, DZMIN, DEFF, SO
 A. ALFDBM = Minimum corium fraction in a cell to initiate the DEBRIS module. (0.60)
 B. PORMAX = Maximum allowable porosity (void fraction) in a bed. (0.55) If a cell in the bed becomes more porous than this value, the code collapses the cell above into it.
 C. DZMIN = Minimum DEBRIS module cell mesh size (0.05 m).
 D. DEFF = Effective particle diameter in the bed (0.10 m).
 E. SO = Specific power (W/kg). This should first be set to the total initial power divided by the total mass of UO_2 . The user should then reduce this value by approximately 20% to account for the release of the volatile fission products (0).

PROBLEM RESTARTS

GENERAL ORGANIZATION

Two data files are required to restart a IFCI calculation, unit 93 (restart file) and unit 95 (input file). As IFCI runs, it creates the file, unit 98, which is a binary file containing restart information. Before running a restart, unit 98 must be copied to unit 93. Then, when IFCI is run in restart mode, unit 93 is used as the reference restart data source.

The user input data file for a restart is unit 95 (the same file name as the problem initial input file) and the input required is similar to that required for the initial problem input. Fluid initialization input is not required. Additionally, several parameters can take the previously set value, by specifying the restart value as 1.1e37. Typically the original input deck is copied without those parts and then modified as necessary.

Restart input data is used to describe the current vessel conditions. It is of three types:

- (1) data that must be entered--such as titles and problem end times,
- (2) data that should be read from the restart file to get its last or original value--such as the time step or mesh size, and
- (3) data that may be either entered or read from the restart.

The flag that tells IFCI to obtain the data for a particular entry from the restart file is the input value 1.1e37. The type of data needed for each of the three types of data in the restart input file is indicated in the input instructions as "enter", as "1.1e37", or as "either" respectively.

GENERAL INPUT

1. ITITLE (20A4) (enter).
 - A. ITITLE = Problem title (up to 80 characters).
2. IRESTRT (enter).
 - A. IRESTRT = The restart switch
 - a. IRESTRT = 1 Read the first restart dump on unit 93, this will correspond to a restart saved at the beginning of step 1.
 - b. IRESTRT = N Read the restart corresponding to step N from unit 93.
 - c. IRESTRT = -1 Read the final restart dump from unit 93. This is typical value for this input.
3. DMPINT, GFINT, EDINT, SEDINT (enter).
 - A. DMPINT = Restart dump interval (sec). (unit 98)
 - B. GFINT = Graphics dump interval (sec). (unit 92).
 - C. EDINT = Full edit interval (sec). (unit 96).
4. PRNTTO (enter)
 - A. PRNTTO = Problem time or step number at which an additional full edit is desired. The logic within the code is such that an input value of 12 would yield a full print at both the 12th step and at 12 seconds.
5. IPRTF, IPRTP, IPRTR, IPRTS, IPRTD (enter).
 - A. IPRTF = FLUIDS module full print flag (0=off, 1=field data, 2=transfer function data, 3=fluid property data).
 - B. IPRTR = RADIATION module full print flag (0=off, 1=on)
 - C. IPRTD = DEBRIS module full print flag (0=off, 1=on).

NOTE: The values chosen for these flags only controls the amount of output sent to unit 96 (text output). If verifying the input set these flags to their maximum value, if little is happening set all flags to 1, if the code is experiencing problems set IPRTF=2.

6. KMAX, NRING (1.1e37).

- A. KMAX = Number of axial mesh nodes
- B. NRING = Number of radial rings
- 7. GASCOEF (either).
 - A. GASCOEF = Maximum fraction of gas internal energy that the gas can receive as a heat source in one time step
- 8. TIME, ENDTIM, DELTO (either).
 - A. TIME = The starting time (sec).
 - B. ENDTIM = Problem end time (sec).
 - C. DELTO = The initial time step (sec). Typically this value is input as 1.1e37 to allow the code to control the time step.
- 9. NTIM (enter).
 - A. NTIM = Number of time step pairs in maximum allowable time step table (> 1).
- 10. STEP(1,n), l=1,2 n=1,NTIM (either).
 - A. STEP = Maximum allowable time step table, NTIM pairs of problem time (seconds) and maximum time step (seconds) Typically, values between 0.25-1.0 are used for the maximum time step. If the code has time step control problems associated with the explicit links between modules the user can lower this value to control the calculation.

FLUID DYNAMICS INPUT

Fluids Module Input: Scalar Data

- 11. DTINC (either).
 - A. DTINC = Maximum allowable fractional time step increase between steps.
- 12. DTMIN (either).
 - A. DTMIN = Minimum time step. Below this value the problem terminates. (sec).
- 13. CRFAC (either).
 - A. CRFAC = Courant multiplication factor.
- 14. ITERMIN, ITERMAX (enter).
 - A. ITERMIN = Minimum number of FLUID module pressure iterations.
 - B. ITERMAX = Maximum number of FLUID module pressure iterations.
- 15. ERROR1 (either).
 - A. ERROR1 = This is the convergence criterion on the change in relative pressure from iteration to iteration. Lowering this value to 1.0e-9 can help provide more stable numerical solutions.
- 16. EPSA (either).
 - A. EPSA = Maximum fractional change in fluid volume fraction between time steps.
- 17. EPST (either).
 - A. EPST = Maximum fractional change in fluid temperature between time step.
- 18. CONDCOE (either)
 - A. CONDCOE = Condensation coefficient multiplies the condensation rate (1.0e-4).
- 19. DCOR3 (either).
 - A. DCOR3 = Particle diameter used in field 3. (m)
- 20. DCOR4 (either).
 - A. DCOR4 = Particle diameter used in field 4. (m)
- 21. FRAC34(l), l=1,8
 - A. FRAC34 = Reference mass fractions for fields 3 and 4. These are the initial mass fractions corresponding to the material id's entered in the initial problem start. The solid/liquid corium equation-of-state (EOS) uses these reference values to determine mass-weighted properties, such as density or heat capacity.
- 22. PREF
 - A. PREF = Reference pressure for fields 3 and 4. The corium thermodynamic EOS uses this parameter (Pa) (see IFCI MODELS AND CORRELATIONS document for the form of the EOS).
- 23. TREF3, TREF4
 - A. TREF3 = Reference temperature for field 3. The solid corium caloric and thermodynamic EOS's use this parameter. (K)

- B. TREF4 = Reference temperature for field 4. Same as above for liquid corium EOS.
(K)
24. ASQ3, ASQ4
- A. ASQ3 = Inverse sound speed squared for field 3. The solid corium thermodynamic EOS uses this parameter. (s^2/m^2)
- B. ASQ4 = Inverse sound speed squared for field 4. The liquid corium thermodynamic EOS uses this parameter. (s^2/m^2)
25. IDETFLG, IDETTRG, IFRAG
- A. IDETFLG = Flag to turn detonation models on or off. 0 = off, 1 = on.
- B. IDETTRG = Detonation trigger/model selector. This selects one of the trigger models and associated detonation model:
- 0 = Pure parametric model, detonation is triggered in cell (JTRG, ITRG) at time TIMTRG (see model- specific input below).
 - 1 = Pressure threshold model, detonation is triggered when pressure in a cell exceeds a trigger pressure threshold.
 - 2 = Pressure/pressure rise rate threshold model, detonation triggers when pressure and pressure rise rate both exceed threshold levels.
- C. IFRAG = Flag to turn fragmentation model on or off. (0 = off, 1 = on)

THE FOLLOWING LINE IS MODEL-SPECIFIC

26. *for IDETTRG = 0:*

JTRG, ITRG, TIMTRG

- A. JTRG = Axial level number for trigger cell.
- B. ITRG = Radial ring number for trigger cell.
- C. TIMTRG = Time at which to trigger (s).

27. *for IDETTRG = 1:*

PTRG

- A. PTRG = Pressure threshold (Pa).

28. *for IDETTRG = 2:*

PTRG, PTRGRAT:

- A. PTRG = Pressure threshold (Pa).
- B. PTRGRAT = Pressure rise rate threshold (Pa/s).

29. DFRAG, TAUFRAG, IHTDET, HTDET

- A. DFRAG = Fine fragment diameter (m).
- B. TAUFRAG = Fine fragmentation time (s).
- C. IHTDET = Fine fragment heat transfer flag, 0 = use standard correlations, 1 = use input parameter HTDET for heat transfer to fine fragments.
- D. HTDET = Fine fragment heat transfer coefficient (W/m^2).

30. IPTS, IIOUT (enter).

- A. IPTS = Number of steps between short FLUID prints (on TTY and unit 96).
- B. IIOUT = For your information print control, edited on short FLUIDS print. (0) A value of:
- 0 = Consecutive edit of all of the values below. (this is the recommended input).
 - 1 = Values of the FLUIDS knobs. a 5 digit number consisting of 0 and 1's, with a 0 indicating that a fluid field is off and a 1 is on. The fields are steam, water, solid corium, liquid corium, and hydrogen. (10001. = all vapor mixture of steam and hydrogen)
 - 2 = Total hydrogen generation rate (kg/s).
 - 3 = Maximum cladding temperature (K).
 - 4 = Maximum heat transfer coefficient between a rod and vapor (W/m^2-K).
 - 5 = Maximum power generation due to oxidation (W/m^3).
 - 6 = Maximum power transferred to either the vapor or the water fields (W/m^3).
 - 7 = Maximum net heat flow between water and vapor (W/m^3).
 - 8 = Maximum pressure in vessel (Pa).
 - 9 = Liquid temperature exiting the vessel (K).
 - 10 = Vapor temperature exiting the vessel (K).
 - 11 = Total steam generation rate (kg/s).

- m. 12 = Volume of liquid water in vessel (m^3).
- n. 13 = Total mass divergence, a measure of the conservation of mass within the FLUIDS calculation. (kg).

Fluids Module Input: Array Data

NOTE: The additive friction factors for each field (vapor, liquid, solid corium, liquid corium) have the following uses:

- (1) To allow or prevent flow between adjacent cells (input 0.0 and $> 1.0\text{e}20$ respectively). This enables the user to model internal structures, which are not explicitly modeled but may restrict axial, or radial, flow.
- (2) To throttle the flow to get the correct cell to cell flow velocities at steady conditions. The FLUIDS module uses cell edge velocities and cell centered pressures, the additive friction factor is: pressure drop / (avg cell height/hydraulic diam) / kinetic energy, where $\text{k.e.} = (0.5 * \rho * \text{vel} * \text{abs}(\text{vel}))$. Typical values for velocities and pressure drops come from either other codes or experimental measurements.

31. NADR

- A. NADR = Number of regions for additive friction factors. Each region will be bounded by ILFT, JBOT, IRIGHT, and JTOP. (1, best to initialize entire problem domain)

NOTE: The following boundaries and axial/radial friction factors are input as a group NADR times, one group for each region.

32. ILFT, JBOT, IRIGHT, JTOP

- A. ILFT = Ring number of first cell on left boundary of region.
- B. JBOT = Axial node number of lowest cell in region.
- C. IRIGHT = Ring number of last cell on right boundary of region.
- D. JTOP = Axial node number of highest cell in region.

NOTE: The radial direction is described by rings, or cells, e.g., RING 1 is bounded by the first radial node (at 0.0) on the interior, and the second radial node on the exterior or right hand side. The axial direction is described by the axial nodes.

33. ADKZ(j,i), j=JBOT,JTOP i=ILFT,IRIGHT

- A. ADKZ = Additive axial friction factor applied at top of axial node J in ring I for field 1, vapor.

34. ADKZ(j,i), j=JBOT,JTOP i=ILFT,IRIGHT

- A. ADKZ = Additive axial friction factor applied at top of axial node J in ring I for field 2, water.

35. ADKZ(j,i), j=JBOT,JTOP i=ILFT,IRIGHT

- A. ADKZ = Additive axial friction factor applied at top of axial node J in ring I for field 3, solid corium. Corium is typically able to melt through most materials and a value $> 1.0\text{e}20$ will prevent it from falling correctly.

36. ADKZ(j,i), j=JBOT,JTOP i=ILFT,IRIGHT

- A. ADKZ = Additive axial friction factor applied at top of axial node J in ring I for field 4, liquid corium. Corium will pour through most plates.

37. ADKR(j,i), j=JBOT,JTOP i=ILFT,IRIGHT

- A. ADKR = Additive radial friction factor applied at right hand face of axial node J in ring I for field 1, vapor.

38. ADKR(j,i), j=JBOT,JTOP i=ILFT,IRIGHT

- A. ADKR = Additive radial friction factor applied at right hand face of axial node J in ring I for field 2, water.

39. ADKR(j,i), j=JBOT,JTOP i=ILFT,IRIGHT

- A. ADKR = Additive radial friction factor applied at right hand face of axial node J in ring I for field 3, solid corium. We assume that walls can inhibit the radial flow of corium.

40. ADKR(j,i), j=JBOT,JTOP i=ILFT,IRIGHT

- A. ADKR = Additive radial friction factor applied at right hand face of axial node J in ring I for field 4, liquid corium.

Fluids Module Input: Boundary Conditions

NOTE: The code assumes that no fluid field can either enter or exit the problem domain (the outer ring and the bottom and top axial nodes). To allow inflow and outflow to the problem domain, the following input is needed. The current version of the code only allows inflow and outflow at the outer boundaries.

41. NINBC

- A. NINBC = Number of cell locations used for inflow boundary conditions (<6).

NOTE: The following inflow boundary condition parameters are repeated as a group NINBC times, one group for each inflow location.

42. INN

- A. INN = For either a top or bottom inflow boundary condition, INN is the radial ring number whose lower interface coincides with the inflow boundary, $1 \leq \text{INN} \leq \text{NRING}$. For an inflow boundary on the right face, $\text{INN} = \text{NRING} + 1$.

43. JIN

- A. JIN = For a right boundary condition, JIN is the axial node number whose outer interface coincides with the inflow boundary, $1 \leq \text{JIN} \leq \text{KMAX}$. For a top boundary condition, this will be $\text{KMAX} + 1$. For a bottom boundary condition, $\text{JIN} = 0$.

44. ARIN

- A. ARIN = Flow area at the inflow boundary (m^2). Typically a mass flow is known and this input is used to relate the known flow to the inlet tables below.

45. NPRIN

- A. NPRIN = Number of entries in inflow pressure condition tables (< 100)

46. NVIN

- A. NVIN = Number of entries in inflow boundary condition velocity tables. (< 100)

47. NTIN

- A. NTIN = Number of entries in inflow boundary condition temperature tables (< 100).

48. NAIN

- A. NAIN = Number of entries in inflow boundary condition volume fraction tables (< 100).

NOTE: The inflow pressure tables are only used to determine the physical properties of the incoming fluid and not the pressure in the problem.

49. PRNTAB(l,n), l=1,2 n=1,NPRIN

- A. PRNTAB = Inflow total pressure table, NPRIN pairs of time (sec) and pressure (Pa).

50. PH2TAB(l,n), l=1,2 n=1,NPRIN

- A. PH2TAB = Inflow hydrogen partial pressure table, NPRIN pairs of time (sec) and pressure (Pa). Must be less than the values in PRNTAB except in the case of a pure noncondensable, in which case $\text{PH2TAB} = \text{PRNTAB}$.

NOTE: The following velocity, temperature, volume fraction and mass fraction inflow tables are input as a group for each of the 4 inflow fields.

51. VINTAB(l,n), l=1,2 n=1,NVIN

- A. VINTAB = Inflow boundary condition velocity table for a field, NVIN pairs of time (sec) and velocity (m/s). Positive velocity direction is from the bottom to the top and from the centerline to the radial boundary. This means that an inflow on a radial boundary has negative values for velocity.

52. TINTAB(l,n), l=1,2 n=1,NTIN

- A. TINTAB = Inflow boundary condition temperature table for a field, NTIN pairs of time (sec) and temperature (K).
53. AINTAB(l,n), l=1,2 n=1,NAIN
 A. AINTAB = Inflow boundary condition volume fraction table for a field, NAIN pairs of time (sec) and fraction. The sum of the volume fractions for all fields should be unity.
54. FRC34(m,k), m=1,ICMPIN k=3,4
 A. FRC34 = Mass fractions of the inflow eutectics. Input mass fraction is input for both fields 3 and 4 if the volume fraction for either field 3 or 4 indicates their presence. If neither field 3 or field 4 will be in the inflow, this input is not read. The value for ICMPIN and the component pattern is determined from the input to MATID3, card 20.
- ****Begin outflow pressure boundary condition section, this pressure is used to determine the pressure within the problem.
55. NPBC
 A. NPBC = Number of locations for outlet pressure boundary condition's (<6)
- Note: The following outflow boundary condition parameters, are repeated as a group NPBC times, one group for each outflow location.
56. MPBC
 A. MPBC = Boundary condition location flag (outer radial = 1, top axial =2).
57. MOUT
 A. MOUT = Axial node for radial outflow pressure boundary condition, if MPBC=1. Radial ring for axial outflow pressure boundary condition, if MPBC=2. This is always on the outside of the mesh, so if MPBC=1 then $1 \leq MOUT \leq KMAX$, and if MPBC=2 then $1 \leq MOUT \leq NRING$. Note that having an inflow and an outflow on the right face of the same cell will cause unrealistic answers.
58. AROUT
 A. AROUT = Outflow area (m^2).
59. HDOUT
 A. HDOUT = Outflow hydraulic diameter (m).
60. NPROUT
 A. NPROUT = Number of entries in outflow pressure boundary condition table (< 100).
61. PROTAB(l,n), l=1,2 n=1,NPROUT
 A. PROTAB = Outflow pressure boundary condition table, NPROUT pairs of time (sec) and pressure (Pa).

STRUCTURES MODULE INPUT

The STRUCTURES module input is used to describe all structure, and place them on the computational mesh. All structures must have at least one surface on a FLUIDS cell interface; this is mandatory. The code allows the user to place structures in their actual locations, thus allowing the code to make reasonable radiation and heat transfer calculations. This module is seldom used.

Structures Module Input: Scalar Data

62. MAXMOD, STCNVG, SFCNVG, ITCRST, ITMELT, IFAILS, NMATMX, NZLOC, NZTIM
 A. MAXMOD = Number of unique structure models to be input. If set = 0, no structure heat transfer nor stress analysis calculation and no additional input is required beyond the 9 values indicated on this card.

RADIATION HEAT TRANSFER MODULE INPUT

The Radiation module input allows the user to control the radiation heat transfer calculation.

63. NGROUP

A. NGROUP = Number of radiation groups (1)

64. ITRMAX

A. ITRMAX = Max number of iterations. (50, for FLUID axial cell heights substantially larger than the radius, 100 or more if they become more comparable in size)

65. RCONV

A. RCONV = Radiation convergence criterion. (1.0e-4, if this error is exceeded by an order of magnitude then ITRMAX should be increased)

66. TBOUND

A. TBOUND = Radiation boundary sink temperature (K).

67. EMISS(k), k=1,6

A. EMISS = Emissivity of structure K. The structures are: rods, outer wall, inner wall, bottom plate, top plate, and debris. (We typically use a value of 0.3 for the solid structures and 0.8 for the debris bed)

68. RFAC, ARHOL, ARHOC, ARHOM

A. RFAC = Planck mean absorption coefficient multiplier for steam. (1.0) Subprogram FKPM provides the value for the coefficient as a function of pressure and temperature, RFAC allows the user to adjust the level.

B. ARHOL = Liquid absorption coefficient. (a typical range is 0.05-0.10)

C. ARHOC = Solid corium absorption coefficient. (0.1, assumes an oxidized surface and high temperatures)

D. ARHOM = Liquid corium absorption coefficient. (0.1)

DEBRIS MODULE INPUT

The DEBRIS module input allows the user to control the model through the formation, meltdown, and existence of the calculation.

69. LDBRIS

A. LDBRIS = DEBRIS module calculation switch. (0=off, 1=on)

70. NZMAX, NBEDM, ICOND

A. NZMAX = Maximum number of nodes in a bed (40-60).

B. NBEDM = Maximum number of beds.

C. ICOND = Effective conductivity model indicator.

a. ICOND = 1, The Imura-Takegoshi/Vortmeyer model is used.

b. ICOND = 2, The Willhite-Kunii-Smith/Luikov model is used.

71. ALFDBM, PORMAX, DZMIN, DEFF, SO

A. ALFDBM = Minimum corium fraction in a cell to initiate the DEBRIS module. (0.60)

B. PORMAX = Maximum allowable porosity (void fraction) in a bed. (0.55) If a cell in the bed becomes more porous than this value, the code collapses the cell above into it.

C. DZMIN = Minimum DEBRIS module cell mesh size (0.05 m).

D. DEFF = Effective particle diameter in the bed (0.10 m).

E. SO = Specific power (W/kg). This should first be set to the total initial power divided by the total mass of UO₂. The user should then reduce this value by approximately 20% to account for the release of the volatile fission products.

7. Appendix B : Stripping Model

A globule of molten core material falling through coolant will most likely be in a state of stable film boiling. The whole globule will be subject to a hydrodynamic force as a result of the relative motion between the globule and the coolant. The tendency of this hydrodynamic force is to deform and fragment the globule except for the stabilizing force of surface tension. The Weber number

$$We = \frac{\rho V^2 d}{\sigma} \quad (B.1)$$

characterizes the ratio of disruptive hydrodynamic force to stabilizing surface tension force.

Experiments indicate that there is a critical value of the Weber number,

$$We_c = 12(1 + 1.077On^{1.6}) \quad (B.2)$$

below which drop breakup will not occur. Here,

$$On = \frac{\mu_d}{(\rho_d D \sigma)^{1/2}} \quad (B.3)$$

is the Ohnesorge number, which characterizes viscous effects on drop breakup. Drop viscosity hinders breakup when On exceeds about 0.1 and effectively prohibits breakup when On exceeds about 2. Viscous effects can be ignored in most situations of interest.

Pilch (1981) suggests that the low viscosity value of the critical Weber number can be interpreted as the condition that one unstable Rayleigh-Taylor wave fits on the windward surface of the deformed drop. Thus, the necessary condition for drop breakup is

$$\frac{D'}{\lambda_c} = 1 \quad (D' = \text{projected drop diameter}) \quad (B.4)$$

where λ_c is the critical Rayleigh-Taylor wavelength in circular coordinates (Drazin 1958),

$$\lambda_c = 2(1.84)D \left[\frac{\sigma}{\rho_d a D^2} \right]^{1/2} = 3.68D \left[\frac{4}{3C_d We} \right]^{1/2} \quad (B.5)$$

The projected diameter (D') of the deformed drop can be written in terms of the eccentricity of an ellipsoid that approximates the shape of the deformed drop:

$$D' = DE^{-1/3} \quad (B.6)$$

where the eccentricity (E) is the diameter ratio of minor axis (B) to the major axis (D'),

$$E = \frac{B}{D'} \quad (B.7)$$

An implicit equation for the critical Weber number is then given by

$$We_c = 18.06 \frac{E^{2/3}}{C_d} \quad (B.8)$$

The expression is implicit because the drag coefficient is a function of the eccentricity, which in turn is a function of

the Weber number. Using Wellek's first expression for the eccentricity (Wellek, 1966) and Clift's expression for the drag on a deformed body (Clift, 1978), the critical Weber number is predicted to be 11.9, which is in excellent agreement with experiment data. The corresponding values of the eccentricity and drag coefficient are 0.511 and 0.968 respectively.

Breakup of the drop is expected when the Weber number exceeds the critical value. For high Weber numbers, Pilch (1981) views breakup as a multistage process in which molten globules break into fragment globules (liquid or solid), and these fragments may further fragment, resulting in a cascade of fragments (liquid or solid), as breakup continues until the Weber number of a fragment drops below the critical value. Decreasing fragment Weber numbers occur because the fragment diameters decrease during breakup and because the relative velocity between the fragment and the flow field decreases (in general). Pilch also concluded that Rayleigh-Taylor instabilities on the windward surface of the drop were responsible for the ultimate fragmentation of the drop.

Pilch (1981) carried out detailed calculations of the breakup process which coupled the dynamic drop deformation and wave growth (including both the linear growth phase and the nonlinear growth phase of Rayleigh-Taylor waves) with droplet acceleration produced by the external flow field. The primary results of this analysis are

1. Unstable surface disturbances will grow and penetrate the drop, producing breakup, in a dimensionless time

$$T_b = \frac{t V_{r,o} \epsilon^{1/2}}{D_o} \approx 1.0 \text{ to } 1.25 \quad (B.9)$$

where

$$\epsilon = \frac{\rho}{\rho_d} \quad (B.10)$$

which is nearly constant over a broad range of Weber numbers, and

2. A small number of fragments is produced from each fragmentation event;

$$N \approx 3 \text{ to } 5.$$

Although Pilch's calculations were carried out primarily for gas/liquid systems ($\epsilon \approx .005$), sensitivity studies showed that T_b and N differed little from the above values when ϵ was as large as 0.1.

Consider one stage of fragmentation, as depicted in Figure B.1.

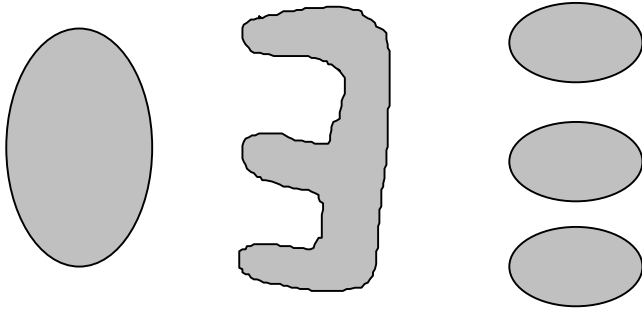


Figure B.1. Single Stage Drop Fragmentation.

The fragment size after the n^{th} stage of fragmentation is

$$d_{n+1} = d_n N^{-1/3} \quad (B.11)$$

and the change in fragment size is given by

$$\Delta d = d_{n+1} - d_n = -d_n(1 - N^{-1/3}) \quad (B.12)$$

which occurs over a single breakup time interval

$$\Delta t = T_b \frac{d_n}{V_{r,n} \epsilon^{1/2}} \quad (B.13)$$

Thus, the instantaneous fragmentation rate is approximated by

$$\frac{\Delta d}{\Delta t} = - \frac{(1 - N^{-1/3})}{T_b} V_{r,n} \epsilon^{1/2} \quad (B.14)$$

Fragmentation is accompanied by an increase in total surface area:

$$\Delta A = A_{n+1} - A_n = N\pi d_{n+1}^2 - \pi d_n^2 = \pi d_n^2 (N^{1/3} - 1) \quad (B.15)$$

The instantaneous source rate of surface area due to fragmentation is then approximated by

$$\frac{\Delta A}{\Delta t} = \frac{(\pi A)^{1/2} (N^{1/3} - 1)}{T_b} V_{r,n} \epsilon^{1/2} \quad (B.16)$$

Keep in mind that use of the constitutive relations (such as those presented here for critical Weber number,

fragmentation rate, and area source rate) are used in large computer codes to provide details of processes whose length scales are too small to be resolved by the computational node size. This implies that the computational node sizes should be large compared to the characteristic particle sizes when using these constitutive relations. If the node sizes were small compared to the particle sizes, then the code should directly compute the dynamics of the fragmentation process and constitutive relations are not needed and should not be used.

The drag coefficient for a deformed or fragmenting drop can be significantly larger than that of an equivalent volume sphere. For increasing values of the Weber number, the equilibrium shape of the deformed drop will progress from a sphere to an oblate spheroid and, in the extreme, resemble a flat disk. The drag coefficient for the deformed shapes will differ from that of a sphere because of shape changes and because the projected area normal to the flow increases with increasing deformation.

Consider first the effect of shape changes on drag coefficients by comparing values for spheres, oblate spheroids, and flat disks that all have the same projected area normal to the flow. Clift et al. (1978) show that differences in the drag coefficient between the various shapes is insignificant for sufficiently small values of the Reynolds number, while at large Reynolds number, the drag coefficient for all shapes can be represented by

$$C_d = .445 [1 + 1.63(1 - E)^2] \quad (B.17)$$

Van Der Leeden et. al. (1956), citing results by Wieselsberger use the expression

$$C_d = .4 \frac{2.78}{1 + 1.78E} \quad (B.18)$$

to calculate the drag on deformed drops. Table B.1 shows that there is no significant difference in the drag coefficients using these two expressions.

Table B.1 Comparison of Drag Coefficient Correlations.

E =	Sphere 1.0	---	Spheroids 0.75 0.5 0.25	---	Disk 0.0
Clift (1978)	0.445	0.49	0.63	0.85	1.17
Van Der Leeden (1956)	0.40	0.48	0.59	0.77	1.11

In computer codes, it is customary to calculate the drag on a deformed or fragmenting drop as if it were a volume equivalent sphere with a modified drag coefficient that accounts for the fact that the deformed drop presents a greater area normal to the flow. The modified drag coefficient (C'_d) is then given by

$$C'_d = C_d E^{-2/3} \quad (B.19)$$

A composite scheme for calculating the drag coefficient of a deformed or fragmenting drop by treating it as a volume equivalent sphere is given by

$$C'_d = E^{-2/3} \text{Max}[C_d(\text{sphere}); C_d(E)] \quad (B.20)$$

Appendix B : Stripping Model

where $C_d(E)$ is either Clift's expression or Van Der Leeden's expression for drag on deformed bodies of equivalent projected area normal to the flow.

The equilibrium eccentricity of a deformed drop decreases with increasing Weber number. An analytic expression derived by Hinze (1949) for small deformations and large Reynolds number ($Re > 500$), when written using current nomenclature, expresses the eccentricity as

$$E = (1 - .0345 We)^{3/2} . \quad (B.21)$$

Hinze's expression is in agreement with the gas/liquid system data ($0.5 < E < 1.0$) of Pruppacher & Pitter (1971) for eccentricities greater than about 0.75, but it predicts an eccentricity that is about 10 % too low when the data shows $E \approx 0.6$. In addition, Hinze's expression yields the unphysical result of negative eccentricity when the Weber number exceeds 29. These shortcomings are to be expected since the expression was derived based on the assumption of small deformations.

Another expression for the eccentricity is given by Wellek et. al. (1966) as

$$E = \frac{1}{1 + .091We^{.95}} , \quad (B.22)$$

which represents an empirical fit to liquid/liquid system data. This expression gives eccentricities that are about 5-10% below the gas/liquid system data of Pruppacher & Pitter (1971). A second expression by Wellek et. al. (1966),

$$E = \frac{1}{1 + .093We^{.98} \left[\frac{\mu}{\mu_d} \right]^{.07}} , \quad (B.23)$$

gives eccentricities that are about 2-5% below the data of Pruppacher & Pitter (1971). The expressions by Wellek et. al. have an advantage for computer applications in that the eccentricity is positive for all values of the Weber number.

The above expressions predict extreme values of the equilibrium deformation for large values of the Weber number. In practice, the drop will break up before

equilibrium deformations are achieved. Fragmentation then provides a lower bound (E_f) on the eccentricity.

Pilch (1981) summarized high Weber number drop deformation data for gas/liquid and liquid/liquid systems. Photographic observations of the fragmenting drops suggest that $E_f \approx 0.125$, but Pilch points out that

photographic data is unreliable at high Weber numbers because surface stripping processes totally obscure the main drop, making the apparent deformation appear much greater than in reality. Pilch (1981) also summarizes reported drag coefficients for fragmenting drops. At high Weber number, the drag coefficient is about 2.5 for both gas/liquid and liquid/liquid systems. This implies that $E \approx 0.19$ using the Van Der Leeden expression or $E \approx 0.21$ using Clift's expression.

A composite scheme for calculating the eccentricity is given by

$$E = \text{Max} [E(\text{Clift or Van Der Leeden}); E_f] \quad (B.24)$$

which can be used for both low and high Weber numbers.

Predictions using the simple models developed here can be compared with experimental data for the fragmentation of single liquid drops in a high velocity gas field. Pilch (1981) has summarized existing data for drop displacement, total breakup time, and resulting fragment sizes. In many of the experiments summarized by Pilch, the drops are suddenly accelerated from rest when a shock wave passes over the drop. Numerical experiments simulating this type of physical experiment have been performed using a computer code that calculates the deceleration of a deformed drop; however, none of the numerical experiments are intended to be an exact replication of any specific physical experiment.

In the numerical experiments, a 1mm water drop (initially stationary) is accelerated suddenly by the flow behind a shock which passes over the drop. The strength of the shock is varied in order to create conditions where the Weber number spans nearly 5 orders of magnitude. The Weber number is based on conditions immediately after the shock passes over the drop. Shock parameters used in the calculations are shown in Table B.2

Table B.2. Air-Water Drops Shock Parameters.

Ma	We	ρ_f	u	U
1.1	59	1.397	55	377
1.3	581	1.811	152	446
1.5	1767	2.228	239	515
2.5	19900	3.98	600	858
4.5	120100	5.751	1226	1544

Table B.3 compares model predictions with experiment data for drop displacement (x), which has been normalized by the initial drop diameter (D_0). Model predictions are higher than the range of experimental data are over the entire range of Weber numbers. The model does, however, demonstrate the same relative increase with

increasing Weber number. Sensitivity of the IFCI code results to this model should be addressed in a thorough validation study. The comparison has been made at the predicted breakup times shown in Table B.4, but model agreement with data is observed at all times.

Table B.3. Normalized Drop Displacement: $x^+ = x/D_0$ Comparison of Model Predictions With Experiment Data

Ma	We	x^+ Model	x^+ Expt
1.1	59	13.2	4.0-8.0
1.3	581	22.8	10.0-20.0
1.5	1767	30.7	12.0-24.0
2.5	19900	45.8	20.0-35.0
4.5	120100	57.3	22.0-40.0

Particle displacements are directly proportional to the drag coefficient and inversely proportional to the particle size. In part, the agreement between model and experiment arises because drag coefficients used in the model were derived from the same drop displacement data to which the model is being compared. However, the agreement also implies that the predicted fragmentation rate and resulting fragment sizes are also in reason with the experimental data. If fragmentation is not considered and the drop is treated as a rigid constant mass sphere with a drag coefficient of 2.5, the predicted drop displacements will be about 30% below current predictions (with fragmentation) at late times.

Model predictions for total breakup time are compared with experiment data in Table B.4. Agreement with experiment data is within about 30%. It should also be noted that at the highest Weber number where there is little data for direct comparison to model predictions. The listed values represent a reasonable extrapolation of a few data points to a slightly higher Weber number. The uncertainty range is characteristic of lower Weber number conditions where experiment data is more abundant.

Table B.4. Normalized Breakup Time, T^+ , Comparison of Model Predictions with Experimental Data

Ma	We	T^+ Model	T^+ Expt
1.1	59	3.4	5.0-6.0
1.3	581	4.2	3.0-4.0
1.5	1767	5.2	4.5-6.5
2.5	19900	6.9	4.5-6.5
4.5	120100	8.4	4.5-6.5

Note : The text refers to the breakup time as T_b , rather than T^+ . T^+ is the usual form for normalized time values.

The model predicts that breakup produces an increasing number of ever smaller fragments, but that all the fragments at any given instant are the same size.

However, a distribution of fragment sizes is observed in the physical process. The experiment data listed in Table B.5 represents the largest stable fragment size observed in

the experiments, which is compared to model predictions. In general, all measures of mean particle sizes from the physical process are less than the maximum stable size;

consequently, the model is likely to underpredict the total surface area.

Table B.5. Normalized Fragment Size, d/D_0 , Comparison of Model Predictions with Experimental Data

Ma	We	d/D_0 Model	d/D_0 Expt
1.1	59	0.4	.01-.03
1.3	581	0.096	0.02-0.1
1.5	1767	0.058	0.01-0.05
2.5	19900	0.024	0.09-0.012
4.5	120100	0.016	0.09-0.012

In summary, predictions using the dynamic fragmentation model compare favorably with experimental data for drop displacement, total breakup time, and final fragment size. This provides confidence that the model provides an adequate representation of the physical process and that the predicted transient size (or total surface area) of particles is reasonably correct.

Pilch (1981) concluded that large-amplitude long-wavelength disturbances were responsible for drop breakup at large Weber numbers. This is the basis for the fragmentation model developed above. However, Pilch also notes that large-amplitude short-wavelength disturbances are subject to wave crest stripping on the windward surface of the drop when the Weber number exceeds about 350. This entrainment from the drop surface is one process that contributes to a distribution of fragment sizes but seems to have a secondary effect on the overall breakup time.

Assume for the moment that entrainment is the only process reducing the size of a given particle. The rate change in the size of the parent drop is proportional to the entrainment rate:

$$\frac{d}{dt} \left[\frac{\rho_d \pi d^3}{6} \right] = -M'' A_s \quad (\text{B.25})$$

$$\frac{dD}{dt} = - \frac{M'' E^{-2/3}}{2\rho_d} \quad (\text{B.26})$$

The eccentricity arises because the deformed drop presents a greater surface area normal to the flow, and the flux of entrained material (M'') from the windward surface of the drop remains to be determined.

Figure B.2 depicts the entrainment process.

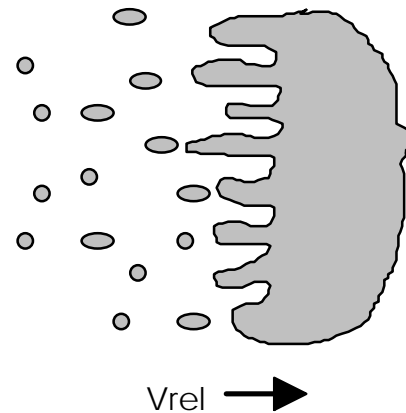


Figure B.2. Rayleigh-Taylor Wave Crest Entrainment.

A small wavelength disturbance grows until its crest-to-trough amplitude (L) is sufficient for surface tension to pinch off a drop, i.e., the troughs connect and the crest is stripped off as a fragment. This occurs when the volume of the finger, approximated as the volume of a cylinder, equals the volume of the entrained fragment

$$\frac{\pi}{4} \left[\frac{\lambda}{2} \right]^2 L = \frac{\pi d^3}{6} \quad (\text{B.27})$$

where the diameter of the fragment is proportional to the diameter of the cylinder

$$d = 1.89 \frac{\lambda}{2} \quad (\text{B.28})$$

Under these conditions, the fragment will pinch off when

$$L = 2.25\lambda \quad (\text{B.29})$$

The entrainment flux is then equal to the mass of the entrained fragment divided by the surface area from which the fragment originated and the time, t_L for the amplitude to reach the value L :

$$M'' = \frac{\rho_d \frac{\pi d^3}{6}}{\frac{\pi}{4} \lambda^2 t_L} = .563 \frac{\rho_d \lambda}{t_L} \quad (\text{B.30})$$

The wavelength of the disturbance leading to entrainment is taken as that of the fastest growing linear phase wave

$$\lambda = \sqrt{3} \lambda_c = 6.37 D \left[\frac{4}{3 C_d We} \right]^{1/2} \quad (\text{B.31})$$

where λ_c is as given before.

The time, t_L , is estimated from the growth rate of a nonlinear Rayleigh-Taylor instability

$$\eta = C_{ss} [a \lambda]^{1/2}, \quad t_L = \frac{L}{\eta} \quad (\text{B.32})$$

where the acceleration, a , is obtained from the Weber-Bond number equivalence as

$$a = \frac{3}{4} C_d \frac{\rho_f V_r^2}{\rho_d D} \quad (\text{B.33})$$

The mass entrainment rate per unit surface area can finally be written as

$$M'' = 0.825 C_{ss} \left(\frac{3}{4} C_d \right)^{1/4} We^{-1/4} (\rho_d \rho_f V_r^2)^{1/2} \quad (\text{B.34})$$

where the empirical constant, C_{ss} , is set to 0.23. This expression for M'' is used in conjunction with equation B.26 to yield,

$$\frac{dD}{dt} = \frac{0.825}{2} C_{ss} \left(\frac{3}{4} C_d \right)^{1/4} We^{-1/4} E^{-2/3} \left(\frac{r_f}{r_d} V_r^2 \right)^{1/2} \quad (\text{B.35})$$

This is the equation for the rate of change of the diameter of the primary drop due to stripping.

The stripping model used compares well to experimental data. The stripping rate is strongly dependent on the adequacy of the models for distortion of the drops and on the drag coefficient correlations used. The errors of this model are generally small, but could be as large as 25 to 30% for some cases. Those instances which might produce those errors are simulations with excessive nodalization refinement, conditions which yield inordinately large drop distortions, or conditions which may yield erroneous drag coefficients.

Appendix B References

- R. Clift, J. R. Grace, and M. E. Weber, 1978, " Bubbles Drops, and Particles, Academic Press.
- P. G. Drazin, 1958, "The Stability of a Shear Layer in an Unbounded Heterogeneous Fluid," J. Fluid Mech., 4, 214-224.
- J. O. Hinze, 1949, " Critical Speeds and Sizes of Liquid Globules," Appl. Sci. Res., AI, 273-288.
- M. Pilch, 1981, "Acceleration Induced Fragmentation of Liquid Drops," Ph. D.dissertation, University of Virginia, Charlottesville, VA.
- H. R. Pruppacher, and R. L. Pitter, 1971, J. Atmos. Sci., 28, 86-94.
- P. Van Der Leeden, L. D. Nio, and P. C. Suratman, 1956, Appl. Sci. Res., Section A 5, 338-348.
- R. M. Wellek, A. K. Agrawal, and A. H. P. Skelland, 1966, AIChE J. 12, 854-862.

DISTRIBUTION LIST

U.S. Nuclear Regulatory Commission
Office of Nuclear Regulatory Research
Washington, DC 20555

ATT: S. Basu NLN344
E. S. Beckjord, NLS007
A. Behbahani, NLN344
Y-S. Chen, NLN344
F. Eltawilla, NL/N344
R. B. Foulds, NL/N344
C. G. Gingrich, NL/N344
T. L. King, NLN370
R. V. Lee, NL/N344
A. Malliakos, NL/N344
A. M. Rubin, NL/N344
B. W. Sheron, NLN369
T. P. Speis, NLS007
C. G. Tinkler, NL/N344
T. J. Walker, NL/N344
R. W. Wright, NL/N344

U.S. Nuclear Regulatory Commission
Office of ACRS
Washington, DC 20555

ATT: M. D. Houston, PHIL P-315

Argonne National Laboratory
RAS, Building 208
9700 South Cass Avenue
Argonne, IL 60439-4842

ATT: D. H. Cho
W. Deitrich
A. Klickman
J. J. Sienicki
B. Spencer
T. Y. C. Wei
A. E. Wright

Battelle Memorial Institute
505 King Avenue
Columbus, OH 43201

ATT: Peter Cybulskis
Richard S. Denning

Experimental Heat Transfer and Fluid Dynamics Group
Department of Nuclear Energy
Building 820M
Brookhaven National Laboratory
Upton, NY 11973

ATT: G. A. Greene
J. Guppy

David A. Ward
David Ward Associates
P.O. Box 6500
North Augusta, SC 29841

Jacek Jedruch
Ebasco Services, Inc.
Two World Trade Center - 89th Floor
New York, NY 10048

Fauske & Associates, Inc.
16W070 West 83rd Street
Burr Ridge, IL 60521
ATT: M. Epstein
H. K. Fauske
R. Hammersley

Mujid Kazimi
Massachusetts Institute of Technology
Department of Nuclear Energy
Building 24, Room 219
77 Massachusetts Avenue
Cambridge, MA 02139

Neil Todreas
Massachusetts Institute of Technology
Department of Nuclear Energy
Building 24, Room 215
77 Massachusetts Avenue
Cambridge, MA 02139

Thomas Kress
Oak Ridge National Laboratory
NRC Programs
P.O. Box X, Bldg. 4500S
Oak Ridge, TN 37831

Anthony P. Malinauskas
Oak Ridge National Laboratory
Mail Stop 6135
Building 4500, Room A170
P.O. Box 2008
Oak Ridge, TN 37831-6135

Michael Podowski
Department of Nuclear Engineering and Engineering
Sciences
Rensselaer Polytechnic Institute
NES Building
Tibbits Avenue
Troy, NY 12180-3590

Distribution

University of California Los Angeles
Nuclear Energy Laboratory
405 Hilgard Avenue
Los Angeles, CA 90024
ATT: Prof. Ivan Catton
Prof. David Okrent

Prof. Theofanis G. Theofanous
University of California
Department of Chemical and Nuclear Engineering
Santa Barbara, CA 93106

Harold L. Dodd
University of Tennessee
Nuclear Engineering Department
315 Pasqua
Knoxville, TN 37996

Prof. Mike L. Corradini
University of Wisconsin
Department of Nuclear Energy
1500 Johnson Drive
Madison, WI 53706

Westinghouse Savannah River Company
New Production Reactor Program
CCC Bldg. 4
1995 South Centennial Avenue
Aiken, SC 29803
ATT: P. L. Gray
L. Hyder
P. Monson
J. P. Morin

Crispin W. Thiessen, Vice President
Westinghouse Savannah River Company
New Production Reactor Program
CCC Bldg. 4
1995 South Centennial Avenue
Aiken, SC 29803

Prof. George E. Apostolakis
38-137 Engineering IV
University of California
Los Angeles, CA 90024-1597

Robert Brodsky
Nuclear Power Technology, Inc.
2018 Turtle Pond Drive
P.O. Box 2969
Reston, VA 22091

J. Roger Hilley
HCR 39, Box 136
Willow Springs, MO 65793-9017

Henry E. Stone
6805 Castlerock Drive
San Jose, CA 95120

U.S. Department of Energy
Idaho Operations Office
785 DOE Place
Idaho Falls, ID 83401-1134

Idaho National Engineering Laboratory
EG&G Idaho, Inc.
P.O. Box 1625
Idaho Falls, ID 83415
ATT: C. M. Allison, MS3840
S. A. Chavez, MS3840
E. A. Harvego, MS3840
J. L. Rempe, MS3840
G. L. Thinnies, MS3740

ABB/CE
1000 Prospect Mill Road
Winsor, CT 06095
CEP 9612-2207
ATT: C. Hoffman
R. Schneider

PLG Inc.
191 Calle Magdalena
Suite 240
Encinitas, CA 92024
ATT: D. Buttermer
J. Reed

Stone and Webster
245 Summer Street
Boston, MA 02107
ATT: James Metcalf, MS245-2

G. E. Knolls Atomic Power Lab.
Box 1072
Schenectady, NY 12501
ATT: John Conine, D2-221

Japan Atomic Energy Research Institute
Tokai-mura, Naka-gun, Ibaraki-ken
319-11
Japan
ATT: Y. Maruyama
J. Sugimoto
N. Yamano

Westinghouse Bettis Atomic Laboratory
P.O. Box 79
West Mifflin, PA 15122
ATT: J. W. Wolfe, ZAP 34N

General Atomics
P.O. Box 85608
San Diego, CA 92138-5608
ATT: S. Inamati

Belgonucleaire
Department of LWR Fuel
Rue de Champde Mars. 25
B-1050 Brussels
Belgium
ATT: H. Bairiot

Whiteshell Laboratories
AECL Research
Reactor Safety Research Division
Pinawa, Manitoba
Canada ROE 1LO
ATT: L. A. Simpson

Kernforschungszentrum Karlsruhe
Postfach 3640
75 Karlsruhe
Germany
ATT: S. Hagen
P. Hofmann

Nucleare e della Protezione Sanitaria (DISP)
Ente Nazionle Energie Alternative (ENEA)
Viale Regina Margherita, 125
Casella Postale M. 2358
I-00100 Roma A. D.
Italy
ATT: G. Petrangeli

Korea Advanced Energy Research Institute
P.O. Box 7
Daeduk-Danji
Taejeon 305-353
Korea
ATT: Hee-Dong Kim

Nuclear Power Engineering Center
Fujitakanko Building
17-1, 3-Chrome, Toranomom, Minato-Ku
Japan, Tokyo 105
ATT: Kenji Takumi

Institute of Nuclear Energy Research
P.O. Box 3
Lungtan
Taiwan 325
Republic of China
ATT: S. I. Chang

Consejo de Seguridad Nuckan
SOR Angela de la Cruz No. 3
Madrid 28056
Spain
ATT: J. Bagues

E. T. S. Ingenieros Industriales
Jost Gutierrez Abascal, 2
28006 Madrid
Spain
ATT: A. Alonso

Statens Karnkraftinspektion
P.O. Box 27106
S-10252 Stockholm
Sweden
ATT: W. Frid

Reactor Centrum Nederland
1755 ZG Petten
The Netherlands
ATT: K. J. Brinkman

UNAEA
Culham Laboratory
Abingdon OX14-3DB
Oxfordshire, England
United Kingdom
ATT: B. D. Turland
D. F. Fletcher

UKAEA
Winfrith, Dorchester DT2-8DH
Dorset, England
United Kingdom
ATT: S. Kinnersly, 203/A32
T. Haste

Consijo De Seguridad Nuclear
Justo Dorado 11
28040 Madrid
Spain
ATT: J. A. Martinez

I. V. Kurchatov Institute of Atomic Energy
Nuclear Safety Department
Moscow, 123182
Russia
ATT: V. Asmolov
V. Strishov

Distribution

Institut de Protection et de Surete Nucleaire
Av. du General Leclerc BP6
92265
Fontenay-aux-Roses
Cedex, France
ATT: G. Cenerino
M. Li Volant

Paul Scherrer Institut
Programm LWR-Sicherheit
CH-5232 Villeggen, PSI
Switzerland
ATT: H. Hirschmann
P. Hosemann
W. Kroeger

Thermodynamics and Radiation Physics
CEC Joint Research Center, Ispra
I-201020 Ispra (Varese)
Italy
ATT: Paola Fasoli-Stella

VATESI
Gediminis Prospect 36
Lithuania
ATT: Povilas Vaisnys

Nuclear Regulatory Authority
Bajkalska 27, 827 21 Bratislava
Slovak Republic
ATT: Josef Misak

Sandia National Laboratories

1 MS0405 D. D. Carlson, 6411
1 MS0736 N. R. Ortiz, 6400
1 MS0737 M. P. Bohn, 6449
1 MS0739 K. E. Washington, 6429
1 MS0739 E. L. Tadios, 6429
10 MS0739 F. J. Davis, 6429
1 MS0742 J. E. Kelly, 6414
1 MS0743 K. D. Bergeron, 6907
1 MS0744 D. A. Powers, 6404
1 MS0744 T. G. Priddy, 6448
1 MS0744 M. J. Rightley, 6403
1 MS0744 W. A. von Reisseman, 6403
1 MS0745 S. L. Thompson, 6418
1 MS0747 A. L. Camp, 6412
1 MS0748 F. T. Harper, 6413
1 MS1137 M. D. Allen, 6422
1 MS1137 C. M. Erickson, 6422
1 MS1137 T. J. Heames, 6422
1 MS1137 M. Pilch, 6422
1 MS1139 K. O. Reil, 6423
1 MS1151 M. Berman, 6515
1 MS1151 K. W. Boyack, 6515
5 MS1151 M. F. Young, 6515

1 MS 9018 Central Technical Files, 8523-2
5 MS 0899 Technical Library, 7141
1 MS 0619 Technical Publications, 7151